A New Model for the Planetary Radiation Pressure Acceleration for Solar Sails

Carzana, Livio; Visser, Pieter; Heiligers, Jeannette

DOI
10.2514/1.G007668

Publication date
2024

Document Version
Final published version

Published in
Journal of Guidance, Control, and Dynamics: devoted to the technology of dynamics and control

Citation (APA)
Carzana, L., Visser, P., & Heiligers, J. (2024). A New Model for the Planetary Radiation Pressure Acceleration for Solar Sails. *Journal of Guidance, Control, and Dynamics: devoted to the technology of dynamics and control*, *47*(8), 1674-1687. https://doi.org/10.2514/1.G007668

JOURNAL OF GUIDANCE, CONTROL, AND DYNAMICS
Vol. 47, No. 8, August 2024

A New Model for the Planetary Radiation Pressure Acceleration for Solar Sails

Livio Carzana,* Pieter Visser,† and Jeannette Heiligers‡
Delft University of Technology, 2329 HS Delft, The Netherlands

https://doi.org/10.2514/1.G007668

Solar sailing is a propulsion method that takes advantage of solar radiation pressure to generate thrust. Although most of near-future solar-sail missions will fly in low Earth orbit, where planetary radiation pressure can be as large as 20% of solar radiation pressure, studies on the accelerations produced by the Earth's albedo and blackbody radiation have only been conducted to a very limited first-order extent. This paper therefore provides a novel, detailed analytical model for these perturbing accelerations, valid for perfectly reflecting solar sails. The full derivation of the model is described, and a thorough analysis of the blackbody and albedo radiation pressure accelerations is conducted for different orbital conditions. Then, to determine the model's accuracy, a comparison with the state of the art (the finite-disk radiation source model and a high-fidelity numerical model) is provided. Ultimately, different analyses to quantify the effect of planetary radiation pressure acceleration on the solar-sail maneuvering capabilities are presented, using NASA's upcoming ACS3 mission as reference scenario. The results highlight the nonnegligible effect of uncontrolled planetary radiation pressure acceleration, which can reduce the sailcraft's achievable altitude and inclination gains to 76 and 80%, respectively, of the gains obtained when planetary radiation pressure is not accounted for.

Nomenclature

A	=	area, m^2
A^*	=	Earth's visible surface as seen from sailcraft
$\boldsymbol{a}$	=	acceleration vector, m/s^2
a	=	semi-major axis, m
a_c	=	solar-sail characteristic acceleration, m/s^2
C_D	=	drag coefficient
C_L	=	lift coefficient
c	=	speed of light, 299,792,458 m/s^2
e	=	eccentricity
f	=	true anomaly, rad
G_F	=	geometrical factor
h	=	altitude, m
I	=	radiation intensity, $W/(sr \cdot m^2)$
i	=	inclination, rad
J_2	=	J_2 spherical harmonics coefficient, $1.082626925639 \cdot 10^{-3}$
L_F	=	latitudinal factor
$\hat{\boldsymbol{n}}$	=	sail normal direction
P	=	radiative power, W
$\mathbb{P}$	=	radiation pressure, N/m^2
R	=	Earth radius, 6,378,136.3 m
$\boldsymbol{r}$	=	orbital radius vector, m
S	=	radiative flux, W/m^2
$\mathbb{S}_\oplus$	=	solar radiative flux at Earth, 1367 W/m^2
$\hat{\boldsymbol{s}}$	=	sunlight direction
V_R	=	atmospheric particle velocity ratio, 0.05
$\boldsymbol{v}$	=	sailcraft inertial velocity, m/s
α	=	solar-sail cone angle, rad
$\alpha_\oplus$	=	solar-sail planetary cone angle, rad
ε	=	error
η	=	subsatellite point's latitude, rad
Λ	=	albedo factor
μ	=	Earth's gravitational parameter, $3.986004415 \cdot 10^{14}$ m^3/s^2
ν	=	shadow factor
ρ	=	atmospheric density, kg/m^3
σ	=	solar-sail loading parameter, kg/m^2
σ_N, σ_T	=	aerodynamic momentum accommodation coefficients, 0.8
Φ	=	albedo phase function
χ^*	=	phase angle, rad
ω	=	argument of pericenter, rad
œ	=	steering law target orbital element

Subscripts

abs	=	absolute
aero	=	aerodynamic
An	=	analytic
avg	=	average
eq	=	equatorial
f	=	final
J_2	=	J_2 spherical harmonics coefficient
out	=	outward-pointing
pol	=	polar
rel	=	relative
sail	=	at sail
0	=	initial

I. Introduction

SOLAR sailing is a low-thrust propulsion method that has raised increasing interest over the last few decades, mainly because of its propellantless nature [1]. In light of its enabling potential for a wide variety of mission scenarios [2,3], extensive research has been conducted on its dynamics and trajectory optimization. Although most of these studies focused on heliocentric flight regimes [3–7], the majority of solar-sail missions to date remained Earth bound [8–12], as will those scheduled for launch in the near future, for example, NASA's Advanced Composite Solar Sail System (ACS3) and Gama's Beta mission [13]. In close proximity of the Earth, the dynamics are much more complex than in interplanetary space because of the presence of eclipses, atmospheric drag, and planetary radiation pressure (PRP). Although multiple studies on the effect of

Presented at the 2022 AAS/AIAA Astrodynamics Specialist Conference, Charlotte, NC, August 7–11, 2022; received 18 April 2023; accepted for publication 14 March 2024; published online 28 May 2024.

*Ph.D. Candidate, Faculty of Aerospace Engineering; L.Carzana@tudelft.nl (Corresponding Author).

†Full Professor, Faculty of Aerospace Engineering; P.N.A.M.Visser@tudelft.nl.

‡Assistant Professor, Faculty of Aerospace Engineering; M.J.Heiligers@tudelft.nl.

aerodynamic drag in low Earth orbit (LEO) have been conducted and showed the enabling capabilities of solar sails for deorbiting purposes [14–18], optimal orbit raising [19,20], and optimal inclination changing [19,21], the accurate derivation of the PRP acceleration and the perturbing effect on the solar-sail dynamics have been investigated to a much lesser extent. Research on this topic has mainly focused on the first-order characterization of the blackbody radiation pressure (BBRP) and albedo radiation pressure (ARP) accelerations and the optimization of planetocentric solar-sail trajectories under these effects [22,23]. In these studies, the models for the BBRP and ARP accelerations are based on the one devised by McInnes [1] and assume the radiating body to be a uniformly bright disk irradiating only in the planet-to-sailcraft direction. Although this assumption correctly approximates the PRP acceleration experienced by sailcraft at large distances from Earth, at low altitudes, a more realistic geometry of the problem and radiation properties of the Earth should be considered to achieve accurate results. Indeed, at low altitudes, the spherical shape of the Earth and the geographical variation of the albedo and blackbody radiation flux play an important role in the modeling of the PRP acceleration. To account for them, several acceleration models have been devised, differing in the formulation adopted (i.e., analytical or numerical), the model employed for the albedo and blackbody radiation flux distributions across the Earth, and the shape of the spacecraft considered. The first works on PRP-acceleration modeling focused mainly on the development of analytical models, particularly by means of approximations through series expansions in the frame of general perturbations methods [24–31]. The use of series expansions based on spherical harmonics increases the complexity of the acceleration equations significantly. As a result, the obtained acceleration formulas are difficult to employ and have limited applicability, especially when compared to currently available numerical models. In fact, these more recent models outperform analytical models in terms of accuracy, although requiring a considerably larger computational effort. These numerical methods are mostly used in software tools for geodetic parameter estimation and precise orbit determination, such as Aerodynamics and Radiation Pressure Analysis (ARPA) [32], NASA's GEODYN [33], ESA's Navigation Package for Earth Orbiting Satellites (NAPEOS) [34], and Delft University of Technology's Near Real-Time Density Model (NRTDM) [35]. To the best of the authors' knowledge, no analytical model exists in the literature that provides a closed-form, analytical solution for the PRP acceleration of a solar sail that does not rely on series expansions, is easy to implement, and achieves a high accuracy. In light of this and the fact that the PRP acceleration can reach a nontrivial magnitude in the order of 10–20% of the solar-sail characteristic acceleration [22], the need for formulating an accurate expression for the PRP acceleration in proximity of the Earth arises. Such an analytical acceleration model would provide a powerful tool to perform high-fidelity orbit analyses for solar-sail LEO missions. Furthermore, it would also lay the foundation for the accurate optimization of Earth-bound steering strategies through (semi-)analytical optimization methods accounting for both the solar radiation pressure (SRP) and PRP accelerations.

In order to fulfill this research need, this paper presents a novel closed-form, analytical model for the BBRP and ARP accelerations of solar sails, found through a sequential surface averaging approach. The model takes into account the complexity of the problem in its entirety as it considers the spherical shape of the emitting body (i.e., the Earth) and accounts for the limited area of the radiating surface as seen from the sailcraft, the geographical dependencies of the albedo and blackbody radiation intensities, the illumination conditions of the radiating surface, and the possibility that both sides of the sail are exposed to the planetary radiation. This model, hereinafter referred to as the *spherical* model, forms an extension of the finite-disk (FD) radiation pressure acceleration model devised by McInnes [1], is valid at any altitude, and can be used for flat-shaped, two-sided reflective solar sails, that is, solar sails with perfectly reflecting front and back sides. In the paper, the assumptions and full derivation of the model are discussed, and analyses are performed to quantify the magnitude of the BBRP and ARP accelerations for different altitudes, sail attitudes, and Sun-planet-sailcraft relative orientations. Then, the model is validated through a thorough error analysis with extensive comparisons against McInnes's FD model and the NRTDM numerical model. Finally, a variety of analyses are presented to assess the effect of the PRP accelerations on the maneuvering capabilities of real-life solar sails in Earth orbit. To this end, the solar-sail orbital dynamics are propagated with and without PRP acceleration using locally optimal orbit-raising and inclination-changing steering laws [19]. In this way, the impact of the uncontrolled PRP acceleration on the maximum achievable altitude and inclination changes is quantified. The analyses are performed considering NASA's ACS3 mission as a reference scenario [13,19]. This solar-sail mission is scheduled for launch in mid-2024 and reflects the currently available technology readiness level of solar-sail missions in LEO.

II. Dynamical Model

The dynamics of a solar sail in proximity to Earth are expressed in an inertial Earth-centered reference frame, $\mathcal{I}(x, y, z)$, with the x axis pointing toward the vernal equinox, the z axis perpendicular to the equatorial plane and pointing toward the north pole, and the y axis completing the right-handed frame. Within this frame the equations of motion of a solar sail can be expressed in vectorial form as

$$\ddot{\boldsymbol{r}} + \frac{\mu}{r^3}\boldsymbol{r} = \boldsymbol{a}_{\mathrm{SRP}} + \boldsymbol{a}_{\mathrm{aero}} + \boldsymbol{a}_{J2} + \boldsymbol{a}_{\mathrm{BBRP}} + \boldsymbol{a}_{\mathrm{ARP}} \tag{1}$$

where the dot notation indicates differentiation with respect to time, $\boldsymbol{r} = [x, y, z]^{\mathrm{T}}$ is the sailcraft position vector, $r = \|\boldsymbol{r}\|$, $\mu = 398,600.4415\ \mathrm{km}^3/\mathrm{s}^2$ is the Earth gravitational parameter [36], and $\boldsymbol{a}_{\mathrm{SRP}}$, $\boldsymbol{a}_{\mathrm{aero}}$, $\boldsymbol{a}_{J2}$, $\boldsymbol{a}_{\mathrm{BBRP}}$, and $\boldsymbol{a}_{\mathrm{ARP}}$ are the SRP, aerodynamic, J_2 gravitational, BBRP, and ARP accelerations, respectively. These accelerations will be described in more detail in the following sections.

It should be noted that, in the analyses presented in the remainder of this paper, only steering laws to increase the semi-major axis and inclination are considered. Although the Earth's J_2 gravitational perturbation has no secular effect on these Keplerian elements [36], other gravitational perturbations with a secular effect on the inclination exist, such as the gravitational accelerations of the Moon and Sun. However, these are orders of magnitude smaller than the accelerations on the right-hand side of Eq. (1), for the orbits considered in this paper [37]. As a consequence, they have not been considered in the equations of motion in order to avoid hampering a clear investigation into the effects of the BBRP and ARP accelerations on the solar-sail orbital dynamics.

A. Solar Radiation Pressure Acceleration

The SRP acceleration is defined assuming a flat, perfectly reflecting sail as per the ideal sail model [1],

$$\boldsymbol{a}_{\mathrm{SRP}} = \nu\, a_c \cos^2\alpha\, \hat{\boldsymbol{n}} \tag{2}$$

where $\nu \in [0, 1]$ is the shadow factor and $\alpha \in [0, \pi/2]$ is the solar-sail cone angle measured between the direction of sunlight $\hat{\boldsymbol{s}}$ and the sail normal direction with no component pointing towards the Sun $\hat{\boldsymbol{n}}$; see Fig. 1a. The shadow factor ν accounts for the effect of eclipses and its value ranges from 0 (no sunlight reaches the sail) to 1 (sail completely

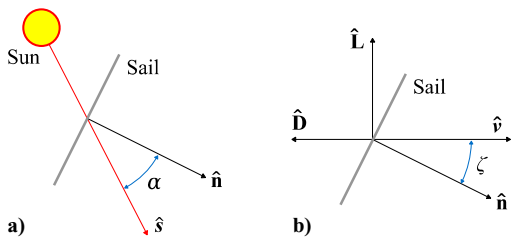

Fig. 1 Solar-sail attitude angles to determine the SRP and aerodynamic accelerations.

illuminated). In this paper, eclipses are modeled using the conical shadow model presented in Refs. [38,39], with the only difference that $\nu = 0$ both when in umbra and penumbra. Finally, a_c represents the SRP characteristic acceleration, that is, the maximum SRP acceleration (achieved for $\alpha = 0$) at a distance of 1 astronomical unit (AU) from the Sun [1]:

$$a_c = \frac{2\mathbb{S}_\oplus}{c\sigma} \tag{3}$$

In Eq. (3), $\mathbb{S}_\oplus = 1367\ \mathrm{Wm}^{-2}$ represents the solar flux at Earth [36], $c = 299{,}792.458$ km/s is the speed of light in vacuum [40], and σ is the sailcraft mass-to-sail area ratio.

B. Aerodynamic Acceleration

The sailcraft aerodynamics are modeled assuming the sail to be a flat plate orbiting at a velocity much larger than the thermal velocity of the atmospheric particles. Under these assumptions, the hyperthermal free-molecular flow model can be used to define the aerodynamic acceleration as [19–21,41,42]

$$\boldsymbol{a}_{\mathrm{aero}} = \frac{\rho v^2}{2\sigma}(C_D\hat{\boldsymbol{D}} + C_L\hat{\boldsymbol{L}}) \tag{4}$$

In Eq. (4), C_D and C_L are the drag and lift coefficients of the sail, v is the sailcraft inertial velocity, and ρ is the atmospheric density, which is modeled using an averaging technique based on the NRLMSISE-00 atmospheric model [19]. The unit vectors $\hat{\boldsymbol{D}}$ and $\hat{\boldsymbol{L}}$ indicate the drag and lift directions, which lie in the same plane formed by the sail normal direction $\hat{\boldsymbol{n}}$ and the sailcraft inertial velocity direction $\hat{\boldsymbol{v}}$, and are antiparallel and perpendicular to $\hat{\boldsymbol{v}}$, respectively (see Fig. 1b). The expressions for C_D and C_L are given by [19–21,41,42]

$$C_D = 2\big[\sigma_T + \sigma_N V_R\big|\cos\zeta\big| + (2 - \sigma_N - \sigma_T)\cos^2\zeta\big]\big|\cos\zeta\big| \tag{5}$$

$$C_L = 2\big[\sigma_N V_R + (2 - \sigma_N - \sigma_T)\big|\cos\zeta\big|\big]\big|\cos\zeta\big|\ \sin\zeta \tag{6}$$

where $\zeta \in [0, \pi/2]$ is the complementary angle to the solar sail's angle of attack (again, see Fig. 1b), σ_N and σ_T are the normal and tangential momentum accommodation coefficients, respectively, and V_R is the ratio of the atmospheric particle average thermal velocity to the sailcraft inertial velocity. Based on Refs. [19–21], $\sigma_N = \sigma_T = 0.8$ and $V_R = 0.05$.

C. J_2 Gravitational Acceleration

The gravitational acceleration due to the Earth's J_2 effect in frame $\mathcal{I}(x, y, z)$ is given by [37]

$$\boldsymbol{a}_{J2} = -\frac{3}{2}\frac{R^2}{r^5}\mu J_2\left[(x\hat{\boldsymbol{x}} + y\hat{\boldsymbol{y}})\left(1 - 5\frac{z^2}{r^2}\right) + z\left(3 - 5\frac{z^2}{r^2}\right)\hat{\boldsymbol{z}}\right] \tag{7}$$

where $\hat{\boldsymbol{x}}$, $\hat{\boldsymbol{y}}$, and $\hat{\boldsymbol{z}}$ are the unit vectors pointing in the $\mathcal{I}(x, y, z)$ frame's x-, y-, and z-axis directions, respectively, $R = 6378.1363$ km is the Earth radius [36], and $J_2 = 1.082626925639 \cdot 10^{-3}$ is the Earth's J_2 gravitational field constant of the Joint Gravity Model 2 (JGM-2) [36,43].

D. Planetary Radiation Pressure Acceleration

To determine the PRP acceleration exerted on a solar sail, it is essential to first establish the amount of planetary radiation received by the sail, define its flux and finally the radiation pressure. If an elementary piece of Earth's surface dA is considered, see Fig. 2a, the amount of power irradiated in a generic direction $\hat{\boldsymbol{l}}$ and enclosed within an infinitesimal solid angle $d\Omega$ is represented by the second differential d^2P as [44]

$$d^2P = I\cos\vartheta\, d\Omega\, dA \tag{8}$$

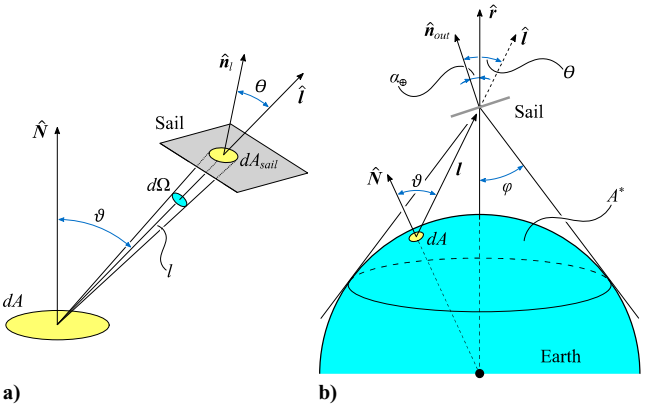

Fig. 2 Geometry of the problem to determine the PRP acceleration.

In Eq. (8), I represents the planetary radiation intensity (across the entire electromagnetic spectrum) along the normal direction to dA, $\hat{\boldsymbol{N}}$, and $\vartheta \in [0, \pi/2]$ is the angle between $\hat{\boldsymbol{N}}$ and $\hat{\boldsymbol{l}}$; see again Fig. 2a. Assuming the Earth's surface to be a Lambertian scatterer, the radiation intensity can be expressed as [45]

$$I = \frac{S}{\pi} \tag{9}$$

where S is the planetary radiation power flux (i.e., the emitted radiation power per unit area) at the surface element dA. When only the radiation received by the solar sail is considered, $d\Omega$ represents the solid angle subtended by an infinitesimal piece of illuminated sail surface dA_{sail}. In this case, $d\Omega$ is defined as [46]

$$d\Omega = \frac{dA_{\mathrm{sail}}\cos\theta}{l^2} \tag{10}$$

where l is the magnitude of the vector $\boldsymbol{l}$ pointing from dA to dA_{sail} and $\theta \in [0, \pi/2]$ is the angle between $\hat{\boldsymbol{l}}$ and the sail normal direction with positive component along $\hat{\boldsymbol{l}}$, $\hat{\boldsymbol{n}}_l$; see Fig. 2a. It should be noted that, depending on the relative orientation of the sail and the surface element dA, $\hat{\boldsymbol{n}}_l$ can either coincide with the sail normal direction pointing away from the Earth, $\hat{\boldsymbol{n}}_{\mathrm{out}}$, as shown in Fig. 2b, or it can be antiparallel to it. Mathematically, this corresponds to

$$\hat{\boldsymbol{n}}_l = \hat{\boldsymbol{n}}_{\mathrm{out}} \cdot \mathrm{sign}\big(\hat{\boldsymbol{l}} \cdot \hat{\boldsymbol{n}}_{\mathrm{out}}\big) \tag{11}$$

Making use of Eqs. (9) and (10), Eq. (8) can be rewritten as

$$d^2P = \frac{S}{\pi}\frac{\cos\vartheta\cos\theta}{l^2}dA_{\mathrm{sail}}\, dA \tag{12}$$

Because this paper considers a flat-shaped solar sail whose dimensions are significantly smaller than l, θ and l can be assumed to be constant across the entire sail surface. This assumption allows one to easily integrate Eq. (12) with respect to dA_{sail} over the entire sail surface A_{sail}, thus yielding the radiation power dP received by the entire sail due to the radiation emitted by dA:

$$dP = \frac{S}{\pi}\frac{\cos\vartheta\ \cos\theta}{l^2}A_{\mathrm{sail}}\, dA \tag{13}$$

The power flux at the sail's location due to the radiation emitted by dA, dS_{sail}, is then found as

$$dS_{\mathrm{sail}} = \frac{dP}{A_{\mathrm{sail}}\cos\theta} = \frac{S}{\pi}\frac{\cos\vartheta}{l^2}dA \tag{14}$$

The corresponding radiation pressure $d\mathbb{P}$ is given by [1]

$$d\mathbb{P} = \frac{dS_{\mathrm{sail}}}{c} = \frac{S}{\pi c}\frac{\cos\vartheta}{l^2}dA \tag{15}$$

so that the infinitesimal PRP acceleration exerted on the perfectly reflecting sail is found as [1]

$$d\boldsymbol{a}_{\mathrm{PRP}} = 2\frac{d\mathbb{P}}{\sigma}\cos^2\theta \;\; \hat{\boldsymbol{n}}_l = \frac{2S}{\pi c\sigma}\frac{\cos\vartheta\cos^2\theta}{l^2}\hat{\boldsymbol{n}}_l\, dA \tag{16}$$

Finally, integration of Eq. (16) over the entire visible surface of the Earth as seen from the sailcraft, A^*, yields the total acceleration exerted on the sailcraft:

$$\boldsymbol{a}_{\mathrm{PRP}} = \frac{2}{\pi c\sigma}\int_{A^*}\left(S\frac{\cos\vartheta\,\cos^2\theta}{l^2}\hat{\boldsymbol{n}}_l\right)\mathrm{d}A \tag{17}$$

It should be noted that Eq. (17) was derived independently of the type of planetary radiation considered. Therefore, this expression is valid for both the BBRP and ARP accelerations, and $\boldsymbol{a}_{\mathrm{PRP}}$ serves as a unifying term to indicate either $\boldsymbol{a}_{\mathrm{BBRP}}$ or $\boldsymbol{a}_{\mathrm{ARP}}$.

The solution to the surface integral of Eq. (17) depends on the Earth-sail geometrical configuration and, most importantly, on the definition of the planetary radiation flux S. Indeed, the planetary radiation flux quantifies the amount of radiation emitted by the surface elements dA across A^*, and its definition depends on whether the blackbody or albedo radiation is considered. To differentiate between the two, in the following, the symbols S_{BBR} and S_{AR} will be used instead of S to refer to the blackbody and albedo radiation fluxes, respectively. Because the amount of radiation emitted by an elementary piece of Earth surface strongly depends on its geographical location, both S_{BBR} and S_{AR} vary across the surface of the Earth following a complex pattern. This renders the integral of Eq. (17) nonelementary, that is, not solvable in terms of elementary functions. To solve this problem, two different approaches have been used in literature to find approximated solutions. The first is to approximate the integrand function of Eq. (17) using Legendre polynomials series expansions (particularly for the planetary flux term S), so as to make the PRP acceleration integral solvable [27,31]. The second is to approximate the PRP acceleration integral by a finite sum over a set of discretized surface elements of the Earth visible from the sailcraft. To apply this method, discrete maps of the geographical distribution of the blackbody radiation flux and albedo coefficient (formally defined later in this section) are required. As an example, Fig. 3 displays the yearly averaged maps of the blackbody radiation flux and albedo coefficient, based on the numerical model of Analysis of Non-Gravitational Acceleration due to Radiation and Aerodynamics (ANGARA) developed by Hyperschall Technologie Göttingen GmbH [47], and used for different applications, spanning from precise orbit determination to parameter estimation [35,48,49]. Although such numerical approaches allow one to achieve accurate results, this comes at the cost of a high computational effort. To derive a closed-form expression for the BBRP and ARP accelerations, this paper uses an analytical approach instead. In particular, a closed-form solution to the integral of Eq. (17) has been found by approximating the planetary flux S with a surface-averaged flux $\overline{S}$, whose definition is given later in this section. By employing $\overline{S}$, the radiation emitted by the visible surface A^* is assumed to be irradiated isotropically, that is, such that any elementary piece of the Earth's visible surface dA emits the same amount of radiation, regardless of its geographical location. Taking advantage of this simplification and using Eq. (11) to express $\hat{\boldsymbol{n}}_l$, an analytical solution to the integral of Eq. (17) can be found, leading to the following expression for the PRP acceleration:

$$\boldsymbol{a}_{\mathrm{PRP}} = \frac{2\overline{S}}{\pi c\sigma}\int_{A^*}\left(\frac{\cos\vartheta\,\cos^2\theta}{l^2}\hat{\boldsymbol{n}}_l\right)\mathrm{d}A = a_{c,\mathrm{PRP}}\, G_F\, \hat{\boldsymbol{n}}_{\mathrm{out}} \tag{18}$$

where $a_{c,\mathrm{PRP}}$ is the PRP characteristic acceleration and $G_F \in [0,1]$ is the so-called geometrical factor. The geometrical factor correlates the Earth-sail geometrical configuration to the PRP acceleration and is defined as

$$G_F = \frac{3}{2\pi}\int_{A^*}\left(\frac{\cos\vartheta\,\cos^2\theta}{l^2}\mathrm{sign}\left(\hat{\boldsymbol{l}}\cdot\hat{\boldsymbol{n}}_{\mathrm{out}}\right)\right)\mathrm{d}A \tag{19}$$

The solution to the surface integral on the right-hand side of Eq. (19) depends on the geometrical configuration of the sail with respect to the Earth, which is uniquely identified by the planetary cone angle (PCA), $\alpha_\oplus \in [0,\pi/2]$, and maximum view angle, $\varphi \in [0,\pi/2]$; see Fig. 2b. The former is defined as the angle between $\hat{\boldsymbol{n}}_{\mathrm{out}}$ and the radial direction $\hat{\boldsymbol{r}}$, while the latter is the angle between the direction pointing to the Earth's tangent as seen from the sailcraft and $-\hat{\boldsymbol{r}}$. Two possible configurations can then be defined:

1) If $\alpha_\oplus + \varphi \le \pi/2$, the incoming radiation from the visible surface A^* illuminates only one side of the sail. In this case, the geometrical factor is equal to

$$G_F(r,\alpha_\oplus) = 1 - \sqrt{1-\frac{R^2}{r^2}}\left[1-\frac{R^2}{r^2}\left(1-\frac{3}{2}\sin^2\alpha_\oplus\right)\right] \tag{20}$$

2) If $\alpha_\oplus + \varphi > \pi/2$, the incoming radiation from the visible surface A^* illuminates both sides of the sail. In this case, each of the two sides of the double-sided reflecting sail provides an acceleration that points either along or opposite to $\hat{\boldsymbol{n}}_{\mathrm{out}}$. Consequently, G_F assumes a more complex expression, given by

$$\begin{aligned} G_F(r,\alpha_\oplus) = 1 - \frac{1}{\pi}\Bigg\{&2\sqrt{1-\frac{R^2}{r^2}}\left[1-\frac{R^2}{r^2}\left(1-\frac{3}{2}\sin^2\alpha_\oplus\right)\right]\sin^{-1}A \\ &+ 2\tan^{-1}B \\ &- 3B^3\cos^4\alpha_\oplus - 2B\cos^2\alpha_\oplus\left(1-\frac{3}{2}\sin^2\alpha_\oplus\right)\Bigg\} \end{aligned} \tag{21}$$

where

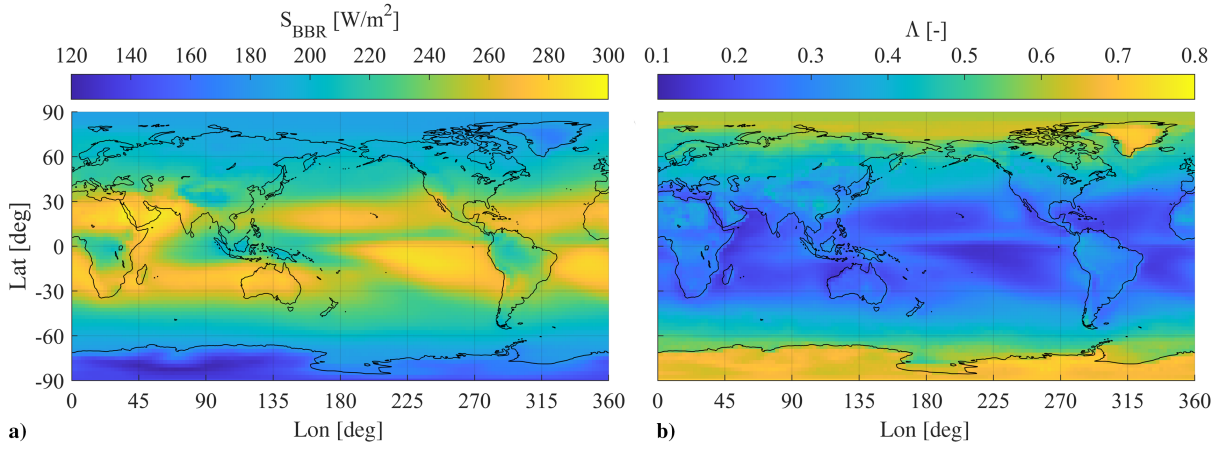

Fig. 3 Yearly averaged maps of the a) blackbody radiation flux and b) albedo coefficient.

$$A = \frac{\cos\alpha_\oplus}{\sin\alpha_\oplus}\sqrt{\frac{r^2}{R^2}-1} \qquad B = \sqrt{\frac{R^2}{r^2\cos^2\alpha_\oplus}-1} \tag{22}$$

The PRP characteristic acceleration is defined as

$$a_{c,\mathrm{PRP}} = \frac{4}{3}\frac{\overline{S}}{c\sigma} \tag{23}$$

Unlike the geometrical factor, the PRP characteristic acceleration depends on the type of radiation considered through the surface-averaged flux $\overline{S}$. Its definition is provided in the following subsections for both the blackbody and albedo radiations. Note that hereinafter the symbols $\overline{S}_{\mathrm{BBR}}$ and $\overline{S}_{\mathrm{AR}}$ will be used instead $\overline{S}$ to refer to the blackbody and albedo radiation fluxes, respectively. In a similar fashion, $a_{c,\mathrm{BBRP}}$ and $a_{c,\mathrm{ARP}}$ will be used instead of $a_{c,\mathrm{PRP}}$ to indicate the BBRP and ARP characteristic accelerations, respectively.

1. Blackbody Flux Model

As shown in Fig. 3a, the blackbody radiation flux S_{BBR} varies across the surface of the Earth following a complex trend. To a first-order level, this trend can be approximated assuming a sinusoidal variation of S_{BBR} with the latitude $\eta \in [-\pi/2, \pi/2]$:

$$S_{\mathrm{BBR}} = S_{\mathrm{BBR,eq}} - \left(S_{\mathrm{BBR,eq}} - S_{\mathrm{BBR,pol}}\right)\sin^2\eta \tag{24}$$

In Eq. (24), $S_{\mathrm{BBR,eq}} = 264.609\ \mathrm{W/m^2}$ and $S_{\mathrm{BBR,pol}} = 173.436\ \mathrm{W/m^2}$ are the reference blackbody radiation fluxes at the equator and the poles. These values have been found by a least-squares fit of the right-hand side of Eq. (24) to the numerical data of the ANGARA yearly averaged flux map of Fig. 3a. Expressing S_{BBR} as in Eq. (24) allows one to define the surface-averaged blackbody radiation flux $\overline{S}_{\mathrm{BBR}}$ analytically as

$$\overline{S}_{\mathrm{BBR}} = \frac{\int_{A^*} S_{\mathrm{BBR}}\,\mathrm{d}A}{\int_{A^*} dA} = S_{\mathrm{BBR,eq}} - \left(S_{\mathrm{BBR,eq}} - S_{\mathrm{BBR,pol}}\right)L_F \tag{25}$$

where $L_F \in [0, 1]$ is the so-called latitudinal factor given by

$$L_F(r,\eta) = \frac{1}{3}\left(\frac{R^2}{r^2}+\frac{R}{r}+1\right) - \frac{1}{2}\frac{R}{r}\left(\frac{R}{r}+1\right)\cos^2\eta \tag{26}$$

Because S_{BBR} varies sinusoidally with latitude, hereinafter this model will be referred to as the *sinusoidal* blackbody flux model. As mentioned before, this model assumes the blackbody radiation to be emitted isotropically, that is, with a constant flux $\overline{S}_{\mathrm{BBR}}$ by the visible surface A^*. However, the flux value depends on the size and location of A^* relative to the equator/poles through the factor L_F. It is worth noting that if $S_{\mathrm{BBR,eq}} = S_{\mathrm{BBR,pol}}$ the sinusoidal variation with latitude is lost, see Eqs. (24) and (25), and $S_{\mathrm{BBR,eq}}$, $S_{\mathrm{BBR,pol}}$, S_{BBR}, and $\overline{S}_{\mathrm{BBR}}$ coincide. In this case, a uniform (i.e., constant) flux distribution across the entire Earth's surface is obtained, and the model is consequently referred to as the *uniform* blackbody flux model. In the reminder of this paper, whenever the uniform flux model is employed, a flux of $S_{\mathrm{BBR}} = 234.732\ \mathrm{W/m^2}$ is used. This value was found by performing a numerical surface average of the flux values of the ANGARA yearly averaged flux map given in Fig. 3a. Because $\overline{S}_{\mathrm{BBR}}$ is constant, $a_{c,\mathrm{BBRP}}$ is also constant, and its value represents the maximum achievable BBRP acceleration, in a fashion similar to the traditional SRP characteristic acceleration a_c. However, this situation occurs only for a nadir-pointing solar sail ($\hat{\boldsymbol{n}}_{\mathrm{out}} = \hat{\boldsymbol{r}}$, $\alpha_\oplus = 0$) at zero altitude, as in this case $G_F = 1$, see Eq. (20), and $\|\boldsymbol{a}_{\mathrm{BBRP}}\| = a_{c,\mathrm{BBRP}}$. Finally, it is worth noting that $a_{c,\mathrm{BBRP}}$ can also be expressed in terms of the SRP characteristic acceleration a_c by substituting Eq. (3) in Eq. (23):

$$a_{c,\mathrm{BBRP}} = \frac{2}{3}\frac{\overline{S}_{\mathrm{BBR}}}{\mathbb{S}_\oplus}a_c = 0.1145\,a_c \tag{27}$$

2. Albedo Flux Model

The albedo radiation flux S_{AR} is defined as [50]

$$S_{\mathrm{AR}} = \Lambda\,\mathbb{S}_\oplus \max(0, \cos\chi) \tag{28}$$

where Λ is the Earth's albedo coefficient, that is, the average amount of solar radiation received by the Earth reflected into space [50] and χ is the sunlight incidence angle between the reverse sunlight direction $-\hat{\boldsymbol{s}}$ and $\hat{\boldsymbol{N}}$; see Fig. 4. The albedo coefficient Λ provides the dependency of S_{AR} on the reflectivity properties of the Earth's surface, which vary following a complex trend; see Fig. 3b. At the same time, the sunlight incidence angle χ provides the dependency of S_{AR} on the illumination conditions of the visible surface A^*, determined by the relative positions of the Earth, Sun, and sailcraft. In light of this, any high-fidelity analytical expressions for S_{AR} assumes a highly nonlinear form, for which the corresponding surface-averaged flux $\overline{S}_{\mathrm{AR}}$ cannot be expressed in terms of elementary functions. To solve this issue, in this paper, different approximations are introduced to express $\overline{S}_{\mathrm{AR}}$ in a closed, analytical form. First, the albedo coefficient is approximated as a sinusoidal function of the latitude η, similar to S_{BBR} in Eq. (24),

$$\Lambda = \Lambda_{\mathrm{eq}} + \left(\Lambda_{\mathrm{pol}} - \Lambda_{\mathrm{eq}}\right)\sin^2\eta \tag{29}$$

where $\Lambda_{\mathrm{eq}} = 0.1854$ and $\Lambda_{\mathrm{pol}} = 0.6149$ are the reference albedo coefficients at the equator and poles. Similar to $S_{\mathrm{BBR,eq}}$ and $S_{\mathrm{BBR,pol}}$, Λ_{eq} and Λ_{pol} have been found by a least-squares fit of the right-hand side of Eq. (29) to the numerical data of the ANGARA yearly averaged albedo map of Fig. 3b. Second, the effect of the albedo and sunlight incidence angle on the albedo radiation flux is uncoupled by approximating the surface-averaged albedo flux $\overline{S}_{\mathrm{AR}}$ with the product of the surface-averaged albedo $\overline{\Lambda}$ and surface-averaged cosine of the sunlight incidence angle Φ. In this way, $\overline{S}_{\mathrm{AR}}$ can be defined as

$$\overline{S}_{\mathrm{AR}} = \frac{\int_{A^*} S_{\mathrm{AR}}\,\mathrm{d}A}{\int_{A^*}\mathrm{d}A} = \mathbb{S}_\oplus\overline{\Lambda}\Phi \tag{30}$$

where

$$\overline{\Lambda} = \frac{\int_{A^*}\Lambda\,\mathrm{d}A}{\int_{A^*}\mathrm{d}A} = \Lambda_{\mathrm{eq}} + \left(\Lambda_{\mathrm{pol}} - \Lambda_{\mathrm{eq}}\right)L_F \tag{31}$$

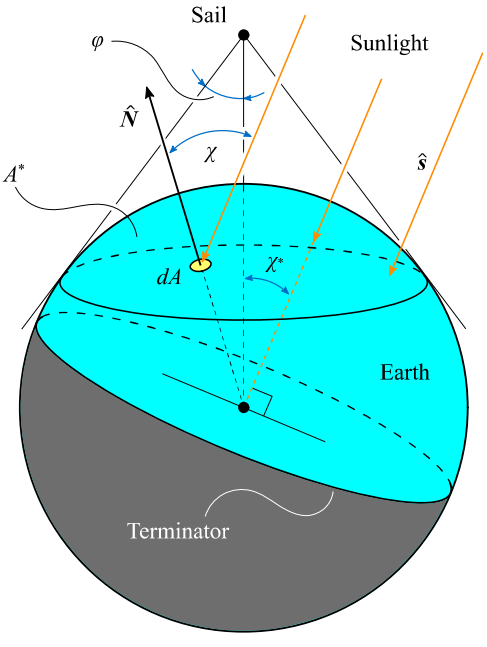

Fig. 4 Geometry of the problem to determine the albedo radiation flux.

$$\Phi = \frac{\int_{A^*} \max(0, \cos\chi)\, \mathrm{d}A}{\int_{A^*} \mathrm{d}A} \tag{32}$$

In the literature, $\Phi \in [0, 1]$ is known as albedo phase function [45] and will be referred to as such in this paper. The phase function accounts for the illumination conditions of the visible surface of the Earth and its expression depends on whether the Earth's visible surface A^* is completely illuminated (if the sailcraft "sees" only the sunlit side of the Earth), partially illuminated (if the Earth's day-night terminator is visible from the sailcraft), or completely dark (if the sailcraft "sees" only the dark side of the Earth). These three cases can be identified through the maximum view angle φ and the phase angle, $\chi^* \in [0, \pi]$, that is, the angle between $\hat{\boldsymbol{r}}$ and the opposite to the sunlight direction $-\hat{\boldsymbol{s}}$; see Fig. 4. For each of these cases, analytical expressions can be found for the phase function Φ, as shown in the following:

1) If $\chi^* < \varphi$, the visible surface A^* is completely illuminated by the Sun. In this case, Φ is equal to

$$\Phi(r, \chi^*) = \frac{1}{2}\left(1 + \frac{R}{r}\right)\cos\chi^* \tag{33}$$

2) If $\varphi < \chi^* < \pi - \varphi$, the visible surface A^* is partially illuminated by the Sun. In this case, Φ is given by

$$\Phi(r, \chi^*) = \frac{1}{2\pi}\left\{\left(1 - \frac{R}{r}\right)^{-1}\left[\cos^{-1}\left(\frac{R}{r\sin\chi^*}\right) - \frac{R}{r}\sqrt{\sin^2\chi^* - \frac{R^2}{r^2}}\right] + \left(1 + \frac{R}{r}\right)\cos\chi^*\cos^{-1}\left(-\frac{R}{\sqrt{r^2 - R^2}}\frac{\cos\chi^*}{\sin\chi^*}\right)\right\} \tag{34}$$

3) If $\pi - \varphi < \chi^*$, the visible surface A^* is completely dark and $\Phi = 0$.

The introduction of $\overline{\Lambda}$ and Φ to separate the dependencies of Λ and χ (and therefore compute $\overline{S}_{\mathrm{AR}}$ analytically) introduces two sources of approximation. Indeed, by employing $\overline{\Lambda}$, a constant albedo coefficient is considered across the entire visible surface A^*, despite the sinusoidal variation with latitude assumed in Eq. (29). Similarly as for $\overline{S}_{\mathrm{BBR}}$, the value of $\overline{\Lambda}$ depends on the size and location of A^* relative to the equator/poles by means of the latitudinal factor L_F. Second, the usage of the phase function Φ implies that all the albedo radiation is emitted isotropically (i.e., uniformly) by the entire visible surface A^*. As a result, the fact that in reality radiation is emitted unevenly and only by the illuminated part of A^* is not taken into account.

Similarly as for the blackbody flux model, it is worth noting that if $\Lambda_{\mathrm{eq}} = \Lambda_{\mathrm{pol}}$ the sinusoidal variation of the albedo with latitude is lost, see Eqs. (29) and (31), and Λ_{eq}, Λ_{pol}, Λ, and $\overline{\Lambda}$ coincide. In this case, a uniform (i.e., constant) albedo distribution across the entire Earth's surface is obtained, and therefore the model is referred to as the *uniform* albedo model. Hereinafter, whenever the uniform albedo model is employed, an albedo coefficient of $\Lambda = 0.3259$ is used. This value was found by performing a numerical surface average of the albedo values of the ANGARA yearly averaged albedo map given in Fig. 3b. By assuming a constant albedo coefficient and substituting Eq. (3) in Eq. (23), $a_{c,\mathrm{ARP}}$ can be expressed as a function of the phase function Φ and the SRP characteristic acceleration a_c as follows:

$$a_{c,\mathrm{ARP}} = \frac{2\Lambda}{3}\Phi\, a_c = 0.2173\Phi\, a_c \tag{35}$$

In the next two sections, different analyses are presented which aim to characterize the BBRP and ARP accelerations achievable in close proximity of the Earth. Here, the discussion will focus mostly on the uniform blackbody flux model and uniform albedo model, unless stated otherwise, for the sake of clarity and easiness of the treatment. The higher-fidelity sinusoidal blackbody flux model and sinusoidal albedo model will be employed later on in the paper, where the validation of the spherical BBRP and ARP acceleration models and the analyses of PRP-perturbed trajectories are discussed.

III. Analysis of Blackbody Radiation Pressure Acceleration

Figure 5 shows the contour plots of the BBRP acceleration magnitude relative to the solar-sail characteristic acceleration a_c in the near-Earth environment, for altitudes up to h = 34,200 km. Two different sail attitudes are considered, namely, a nadir-pointing solar sail (i.e., $\hat{\boldsymbol{n}}_{\mathrm{out}} = \hat{\boldsymbol{r}}$) and inertial-pointing solar sail (chosen to point along the x axis, $\hat{\boldsymbol{n}}_{\mathrm{out}} = \pm\hat{\boldsymbol{x}}$, without loss of generality). As can be seen in Fig. 5a, for a nadir-pointing attitude, the BBRP acceleration magnitude a_{BBRP} depends solely on the orbital altitude h as the PCA is constantly equal to zero. This allows correlating a_{BBRP} and h, as shown in the legend of Fig. 5a. The contour plot shows the rapid decay of a_{BBRP}, especially at low altitudes. This is because each elementary piece of Earth's visible surface dA emits radiation whose power intensity dP decreases as an inverse square law of the distance from the sail l; see Fig. 2a and Eq. (13). Although increasing the altitude also extends the size of the visible surface of the Earth (that is, the size of the surface emitting radiation) A^*, the inverse-square-law decay of the radiation intensity remains dominant. As a result, a_{BBRP} declines swiftly, displaying a behavior similar to an inverse square law. Nevertheless, the contour plot shows that accelerations even up to 11% of a_c can be achieved for low altitudes, which is in agreement with Eq. (27) and in line with the results found in the literature [22]. Similar to Fig. 5a, Fig. 5b shows the iso-acceleration curves for an inertial-pointing solar sail, with the sail normal pointing along the x axis. In this case, the acceleration varies less uniformly as the PCA is not constant. In particular, a_{BBRP} is equal to zero on the z axis; this is because the sail is oriented edgewise with respect to the radial direction ($\alpha_{\oplus} = \pi/2$), therefore causing the BBRP accelerations exerted on the sail's front and back sides to counteract each other. Also, it is worth noting that the acceleration profile is symmetric with respect to the z axis, which is a consequence of the fact that a double-sided perfectly reflecting solar sail has been considered. Indeed, for a

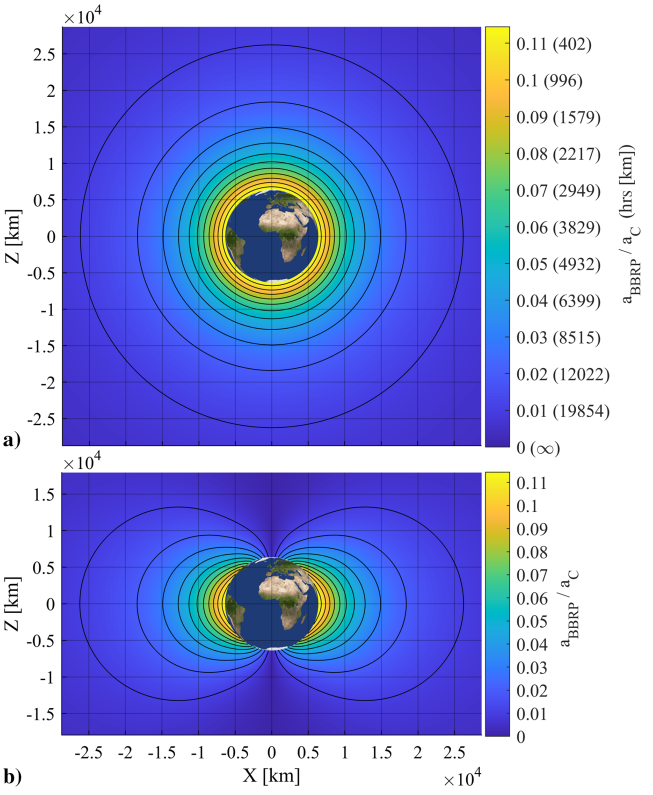

Fig. 5 BBRP acceleration for a) nadir-pointing and b) inertial-pointing solar sails (spherical uniform model).

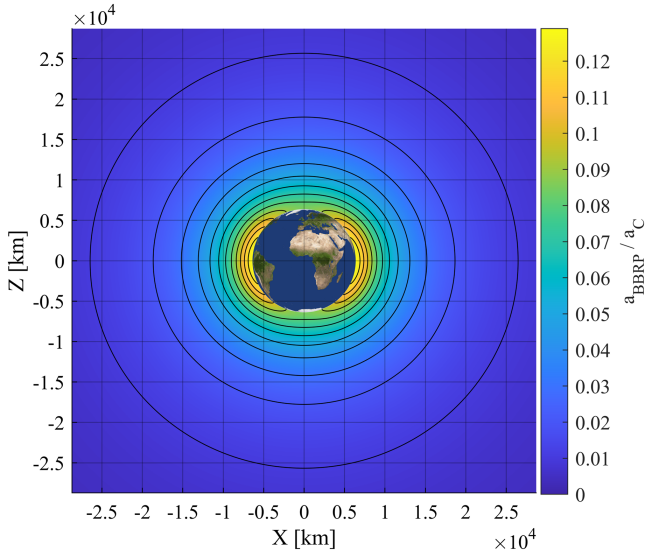

Fig. 6 BBRP acceleration for a nadir-pointing solar sail (spherical sinusoidal model).

solar sail with different optical properties on the front and back sides, no symmetry would be found.

The results presented earlier in this section considered a spherical uniform PRP acceleration model. To gain insight also into the spherical sinusoidal model, Fig. 6 displays the sinusoidal model's distribution of the BBRP acceleration magnitude around the Earth for a nadir-pointing solar sail, considering altitudes up to $h = 34{,}200$ km. Unlike the uniform model's distribution of Fig. 5a, the sinusoidal model's distribution shows no spherical symmetry, only an axial symmetry along the Earth's polar axis. This is due to the latitudinal variation of the BBRP acceleration magnitude introduced by the latitudinal factor L_F; see Eq. (26). The latitudinal variation of a_{BBRP} is especially evident at low altitudes as it creates an equatorial bulge in the acceleration magnitude distribution with a maximum value of almost 13% of a_c. On the other hand, a smaller acceleration magnitude is achieved at the poles, where a_{BBRP} reaches at most 8.4% of a_c. Finally, it is worth noting that for increasing altitudes the contour lines circularize, meaning that a spherical symmetry is found and the sinusoidal model tends to the uniform model.

IV. Analysis of Albedo Radiation Pressure Acceleration

Similar to Fig. 5 for the BBRP acceleration, Fig. 7 shows the variation of the ARP acceleration magnitude a_{ARP} relative to the characteristic acceleration a_c for a nadir-pointing and Sun-pointing solar sail and for altitudes up to $h = 39{,}600$ km. Although for the BBRP acceleration the relative position of the Sun with respect to the sail was not of any importance, it is for the ARP acceleration. In both plots of Fig. 7, the Sun is placed along the positive x axis, and therefore the direction of sunlight is $\hat{s} = -\hat{x}$. Compared to the BBRP acceleration, the variation of the ARP acceleration around the Earth for a nadir-pointing sail displays a more complex pattern, due to the additional dependency of a_{ARP} on the phase angle χ^*. Indeed, Fig. 7a shows that large ARP accelerations are achieved when the sail is above the sunlit side of the Earth, reaching values up to 21% of the characteristic acceleration for low altitudes and $\chi^* = 0$ (subsolar point, on the positive x axis), in agreement with Eq. (35). The ARP acceleration decreases rapidly when moving toward the dark side of the Earth, and, notably, the acceleration contour lines assume a high curvature in proximity of the terminator. This highlights that a_{ARP} does not decrease monotonically with altitude in this region, which is due to two counteracting effects: although for increasing altitudes the intensity of the radiation emitted by the Earth decreases, a higher altitude also allows the illuminated part of the Earth visible from the sailcraft to be larger, thus making the sail receive more albedo radiation. Because this latter effect is predominant at low altitudes, an increase in altitude initially yields a larger a_{ARP}. However, for even

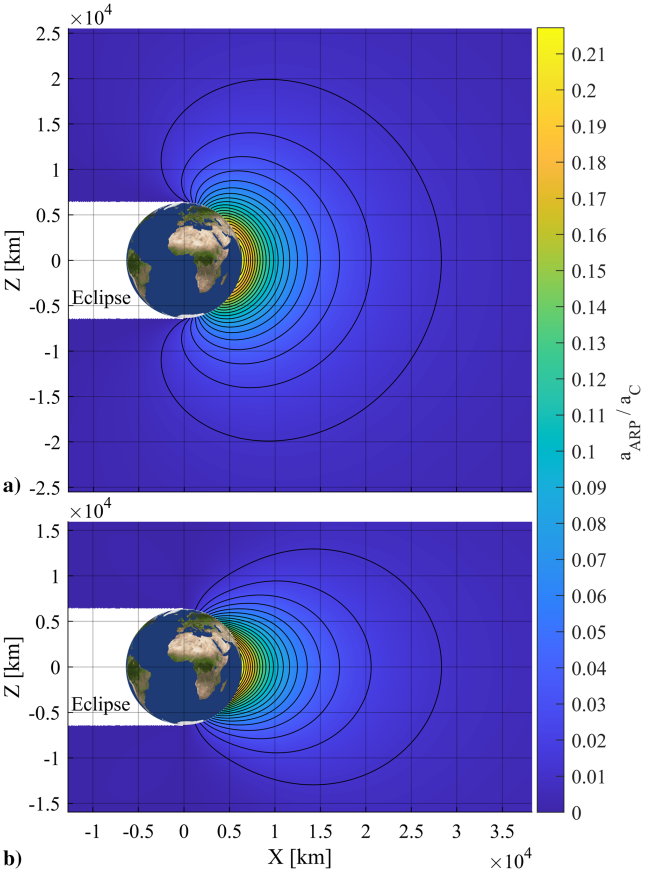

Fig. 7 ARP acceleration for a) nadir-pointing and b) Sun-pointing solar sails (spherical uniform model).

larger altitudes, the radiation intensity decreases rapidly and its effect becomes predominant, hence making a_{ARP} decrease as well. Similar to Fig. 5a, Fig. 7b displays the variation in ARP acceleration for a Sun-pointing solar sail. In this case, the region of high ARP acceleration shrinks, because moving toward the dark side of the Earth yields increasingly larger PCAs that negatively affect the ARP acceleration magnitude.

To gain insight into the ARP acceleration as per the spherical sinusoidal model, Fig. 8 displays the sinusoidal model's distribution of the ARP acceleration magnitude around the Earth, for altitudes up to $h = 39{,}600$ km, for a nadir-pointing solar sail, and assuming the

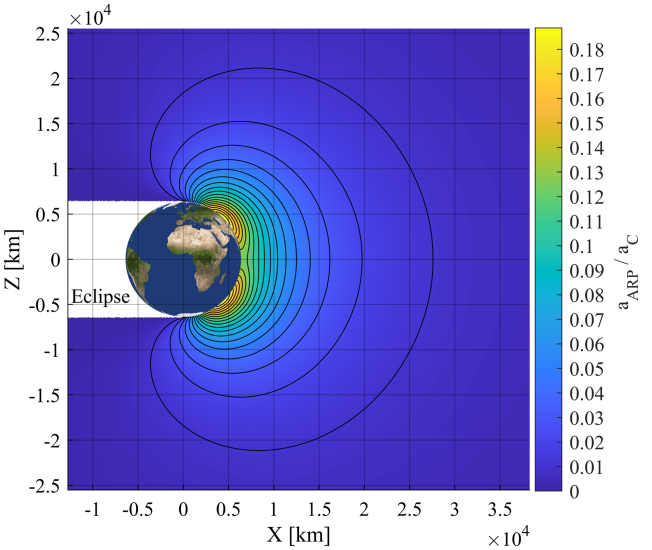

Fig. 8 ARP acceleration for a nadir-pointing solar sail (spherical sinusoidal model).

Sun to be in the equatorial plane (along the positive x axis). Comparison of Figs. 7a and 8 shows that the accelerations of the uniform and sinusoidal models vary similarly at large distances from the Earth, while differences arise at low altitudes. Indeed, the largest ARP acceleration magnitude in the sinusoidal model is about 19% of a_c and it is found at intermediate latitudes. The reason behind this peculiar acceleration magnitude distribution is twofold. On the one hand, the surface-averaged albedo radiation flux $\overline{S}_{\mathrm{AR}}$ tends to decrease when moving away from the subsolar point, as the phase function Φ assumes increasingly lower values; see Eqs. (30) and (33). On the other hand, because in the sinusoidal model the albedo coefficient increases with latitude, the albedo radiation flux tends to increase when moving away from the equator; see Eqs. (29–31). These two effects work in opposite directions, thereby resulting in an acceleration distribution with a maximum magnitude at intermediate latitudes.

V. Comparison with State of the Art

This section presents several analyses that aim to measure the accuracy of the spherical PRP acceleration model compared to other models in the state of the art. In particular, Sec. V.A provides a comparison with the FD model devised by McInnes [1], and Sec. V.B presents different parametric analyses to validate the spherical model by measuring its accuracy relative to a high-fidelity numerical model.

A. Comparison with Finite-Disk Radiation Source Model

The FD model has been widely applied in the literature [22,23] and assumes the emitting body (the Earth) to irradiate as a uniformly bright disk solely in the radial direction $\hat{\boldsymbol{r}}$. As such, it does not take into account the curvature of the Earth and the possibility of having both sides of the sail illuminated simultaneously. Similar to the spherical uniform model, the FD model also assumes a constant blackbody radiation flux and albedo coefficient. In light of this, in the following subsections, the FD model will be compared against the spherical uniform model, rather than the spherical sinusoidal model. In this way, the differences arising from the different geometrical assumptions underlying the FD and spherical uniform models will be better highlighted.

1. *Blackbody Radiation Pressure Acceleration*

When using the FD model, the BBRP acceleration $\boldsymbol{a}_{\mathrm{BBRP,FD}}$ can be expressed as [1,22,23]

$$\boldsymbol{a}_{\mathrm{BBRP,FD}} = a_{c,\mathrm{BBRP}}\, G_{F,\mathrm{FD}}\, \hat{\boldsymbol{n}}_{\mathrm{out}} \tag{36}$$

where $G_{F,\mathrm{FD}}$ represents the geometrical factor of the FD model:

$$G_{F,\mathrm{FD}} = \left[1 - \left(1 - \frac{R^2}{r^2}\right)^{3/2}\right] \cos^2 \alpha_{\oplus} \tag{37}$$

The only difference between the BBRP accelerations of the spherical uniform model and FD model is given by the definition of the geometrical factors; see Eqs. (18) and (36). For this reason, the comparison of the BBRP accelerations of these two models also provides direct insights in the difference between G_F and $G_{F,\mathrm{FD}}$.

Figure 9 displays a comparison between the acceleration envelope curves of the spherical and FD models for a range of altitudes. These curves represent the set of all attainable BBRP accelerations achievable when changing the PCA. As can be seen, both models provide the same BBRP acceleration when $\alpha_{\oplus} = 0$. This is because, for $\alpha_{\oplus} = 0$, the spherical and FD models' geometrical factors are identical; see Eqs. (20) and (37). For increasing PCAs, discrepancies between the acceleration envelope curves arise, particularly in the transversal direction (i.e., perpendicular to $\hat{\boldsymbol{r}}$). These differences depend on the altitude considered because for increasingly larger altitudes the approximation introduced by considering the planet as a uniformly irradiating disk rather than a spherical radiation source reduces. Consequently, the spherical model's envelope curve converges to the FD model's envelope curve for $h \to \infty$. Because the

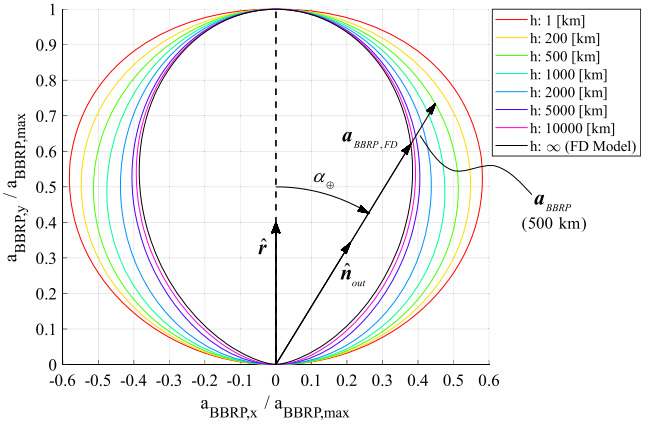

Fig. 9 BBRP acceleration envelope curves of the FD and spherical models.

spherical model's envelope curve depends on the altitude and exhibits a larger transversal component compared to the FD model's envelope curve, the largest acceleration differences between the two models are found for low altitudes and intermediate values of the PCA (45–75 deg), reaching values even in the order of 3–4% of the characteristic acceleration a_c.

2. *Albedo Radiation Pressure Acceleration*

Similarly as for the analysis for the spherical BBRP acceleration model, the accuracy of the spherical uniform ARP acceleration model is quantified by comparing it against the FD ARP acceleration model. The ARP acceleration of the FD model can be expressed as [1]

$$\boldsymbol{a}_{\mathrm{ARP,FD}} = a_{c,\mathrm{ARP,FD}}\, G_{F,\mathrm{FD}} \hat{\boldsymbol{n}}_{\mathrm{out}} \tag{38}$$

where $a_{c,\mathrm{ARP,FD}}$ is the albedo characteristic acceleration of the FD model. Similar to Eq. (35) for the spherical uniform model, $a_{c,\mathrm{ARP,FD}}$ can be defined in terms of the SRP characteristic acceleration a_c as

$$a_{c,\mathrm{ARP,FD}} = \frac{2\Lambda}{3} \Phi_{\mathrm{FD}}\, a_c = 0.2173\, \Phi_{\mathrm{FD}}\, a_c \tag{39}$$

where Φ_{FD} is the albedo phase function of the FD model, given by

$$\Phi_{\mathrm{FD}} = \max\left(0, \cos\chi^*\right) \tag{40}$$

The given definition of $a_{c,\mathrm{ARP,FD}}$ is based on albedo flux models commonly used in the literature [22,50] and differs from $a_{c,\mathrm{ARP}}$ only for the use of Φ_{FD} instead of Φ; see Eqs. (35) and (39).

The different definitions of the geometrical factor and phase function of the spherical and FD models are at the core of the acceleration differences between the two models. Different geometrical factors determine different shapes of the ARP acceleration envelope curves, in a fashion similar to the BBRP acceleration envelope curves of Fig. 9. On the other hand, the albedo phase functions affect the maximum achievable ARP accelerations of the two models, so different phase functions translate into different dimensions of the ARP acceleration envelope curves. To provide insights into this difference, Fig. 10 displays the albedo phase functions of the two models. As can be observed, the spherical model's phase function depends on altitude, unlike the FD model's phase function, in agreement with Eqs. (33), (34), and (40). Furthermore, it is interesting to note that, while the geometrical factor of the spherical model converges to that of the FD model for increasing altitudes, see Fig. 9, the opposite is true for the phase function. Indeed, the spherical model's phase function Φ and FD model's phase function Φ_{FD} coincide for $h = 0$. Then, for increasing altitudes, the difference between Φ and Φ_{FD} (and, therefore, between the sizes of the acceleration envelope curves) increases steadily, reaching values even in

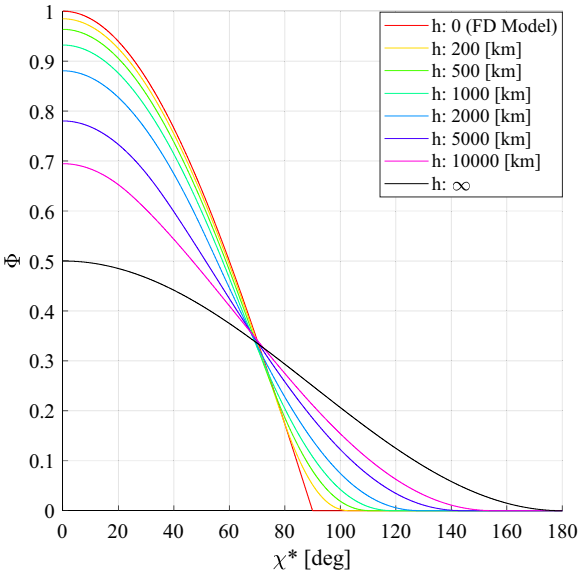

Fig. 10 Albedo phase functions of the FD and spherical models.

the order of 0.05–0.10 for altitudes in the range 500–1000 km and a maximum of 0.5 for $h \to \infty$.

B. Parametric Analyses

In this section, different parametric analyses are presented which aim to validate the spherical PRP acceleration model and quantify its accuracy compared to a high-fidelity numerical model. To achieve this, a wide variety of PRP-perturbed, Earth-bound orbits have been propagated using different PRP acceleration models. The equations of motion employed are given in Eq. (1), but with $\boldsymbol{a}_{\text{aero}} = \boldsymbol{a}_{J2} = \boldsymbol{0}$, that is, excluding the effect of aerodynamic drag and J_2 gravitational accelerations. These terms have been neglected as they would have introduced additional perturbations in the dynamics, thus making it more difficult to clearly determine the accuracy of the different PRP acceleration models. The PRP acceleration models considered are as follows:

1) The PRP acceleration model implemented in the software tool near real-time density model (NRTDM), which computes the BBRP and ARP accelerations by approximating the acceleration integral of Eq. (17) with a finite sum. NRTDM is a software tool developed at the Delft University of Technology under ESA contract whose results have been used for different applications, including precise orbit determination, parameter estimation for the ERS and ENVISAT satellites, and processing of the GOCE and Swarm satellites' measurements [35,48,49]. To model the planetary flux distribution across the Earth, this model makes use of two monthly averaged maps, one for the blackbody radiation flux and one for the albedo coefficient, similar to the yearly averaged maps of Fig. 3. These maps have been obtained from the ANGARA software package developed by Hyperschall Technologie Göttingen GmbH [47], and they have been created based on the satellite data collected across the 1980s by the Earth Radiation Budget Experiment (ERBE) mission [35]. Thanks to the fine angular resolution of 2.5×2.5 deg^2 and the fact that a monthly variability is considered in the maps, this model allows one to determine the BBRP and ARP accelerations to a very high accuracy, although requiring a large computational effort. For more information on NRTDM, the reader is referred to Ref. [35].

2) The spherical model with uniform blackbody radiation flux/albedo distributions, see Secs. II.D.1 and II.D.2.

3) The spherical model with sinusoidal blackbody radiation flux/albedo distributions, see Secs. II.D1 and II.D.2.

4) The finite-disk model, see Secs. V.A.1 and V.A.2.

5) A model neglecting the PRP acceleration altogether, that is, $\boldsymbol{a}_{\text{BBRP}} = \boldsymbol{a}_{\text{ARP}} = \boldsymbol{0}$ at any time.

All analyses make use of the ACS3 mission orbit as baseline scenario, with a solar-sail characteristic acceleration of $a_c = 0.045$ mm/s^2 and the following vector of initial orbital elements defined in frame $\mathcal{I}(x, y, z)$:

$$[a_0, e_0, i_0, \text{LTAN}_0, \omega_0, f_0]^T = \left[7093.1363 \text{ km}, 0, 98.2490 \text{ deg}, \begin{Bmatrix} 00{:}00 \text{ AM} \\ 00{:}30 \text{ AM} \\ \vdots \\ 11{:}30 \text{ PM} \end{Bmatrix}, 0 \text{ deg}, 0 \text{ deg} \right]^T \tag{41}$$

where a is the semi-major axis, e is the eccentricity, i is the inclination, ω is the argument of perigee, f is the true anomaly, LTAN stands for local time of the ascending node, and the subscript 0 denotes the initial value of these variables.[§] These orbital elements represent a circular, Sun-synchronous orbit with initial altitude $h_0 = a_0 - R = 715$ km. In Eq. (41), several values of the LTAN are considered, spaced by 0.5 hrs along the entire 24-hour time span. This parameter defines the orbit orientation in frame $\mathcal{I}(x, y, z)$ and is equivalent to the right ascension of the ascending node, which, in a similar fashion, is spaced by 7.5 deg across the entire 360 degrees angular span. The parametric analysis also considers 12 different simulation start times, corresponding to the 15th day of each month of 2023. For each initial orbit, the solar-sail dynamics are propagated while implementing locally optimal orbit-raising and inclination-changing steering laws. These steering laws are computed using an algorithm devised by McInnes [1], accounting only for SRP in the optimization process. Therefore, the BBRP and ARP accelerations are considered as uncontrolled perturbing accelerations affecting the orbit. For each initial orbit, each simulation start time, and each steering law, five different propagations are performed in which the PRP acceleration is computed through the five models listed previously. Then, the relative errors between the final altitude/inclination obtained by the NRTDM model (taken as the ground truth) and each of the analytical models, ϵ_{rel}, are computed. The parameter ϵ_{rel} is used as metric of the accuracy of the analytical models, and it is defined as

$$\epsilon_{\text{rel}} = \frac{\left| \text{oe}_{\text{NRTDM},f} - \text{oe}_{An,f} \right|}{\text{oe}_{\text{NRTDM},f} - \text{oe}_0} \tag{42}$$

where oe_0 indicates the initial value of the steering law's target parameter (i.e., h or i) and $\text{oe}_{\text{NRTDM},f}$ and $\text{oe}_{An,f}$ represent the final values of the target parameter found through the NRTDM and the analytical model under consideration, respectively. For each simulation, the dynamics have been propagated for 10 days, using MATLAB®'s ode45 integrator with absolute and relative tolerances of 10^{-12}. The analysis settings presented will be used as reference settings in the following subsections to investigate the accuracy of the spherical models and its variation with the initial LTAN, altitude, and inclination.

1. *Variation in Accuracy Due to LTAN*

Figure 11 shows the variation of the relative error with the LTAN for the orbit-raising steering law for all analytical models. For each model, a band is displayed which represents the range of relative errors obtained by considering simulation start times at different months. All the error bands follow a 12-hour periodic trend, approximately symmetric with respect to the LTAN at 1200 hrs. This is due to the relative orientations of the Sun-synchronous orbits with respect to the direction of sunlight, which can be similar even for different LTANs and therefore yield similar errors ϵ_{rel}. When the PRP is neglected or the FD model is used, the relative errors approach a

[§]The ACS3 mission data were taken from personal communication with W.K. Wilkie, Principal Investigator of the ACS3 mission, NASA Langley Research Center, February 2023.

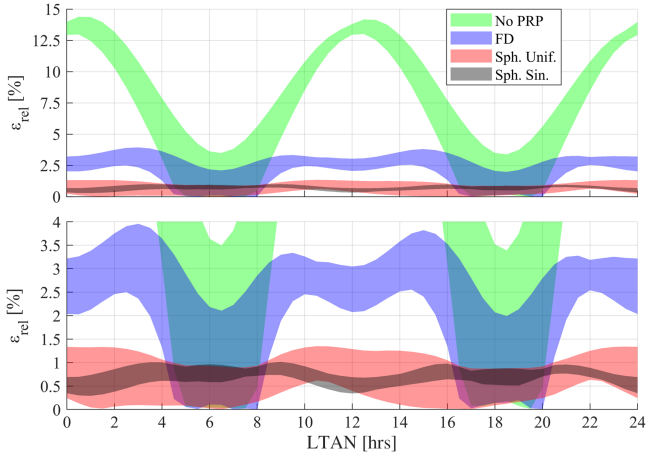

Fig. 11 Relative error on the altitude increase of different analytical PRP acceleration models.

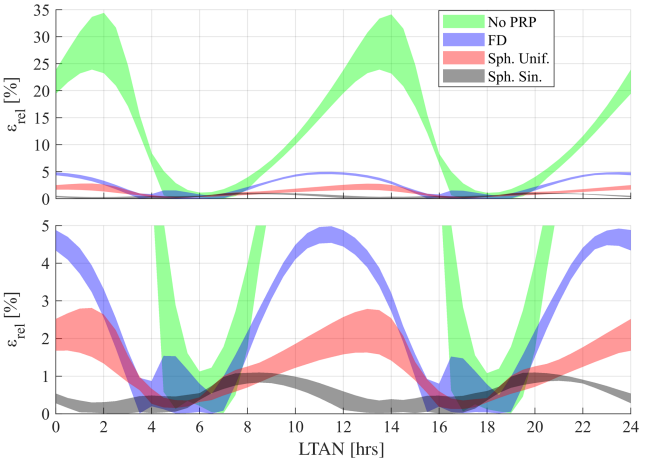

Fig. 12 Relative error on the inclination increase of different analytical PRP acceleration models.

minimum for a LTAN at 0600/1800 hrs (corresponding to a dawn-dusk orbit). The reason for this is that the phase angle χ^* is always close to 90 deg and therefore a very small ARP acceleration is exerted on the sail; see Figs. 7 and 8. Furthermore, by implementing the orbit-raising steering law, the sail is constantly oriented almost edgewise with respect to the radial direction. This corresponds to a PCA $\alpha_\oplus$ approximately equal to 90 deg at all times and thus a minor BBRP acceleration; see Figs. 5b and 9. When a LTAN at 0000/1200 hrs is considered (corresponding to noon-midnight orbits), the BBRP and ARP accelerations are the largest, and therefore the errors ε_{rel} achieved by these two models are maximum. This result is due to the fact that the sailcraft flies in the vicinity of the subsolar point once per orbit, where the ARP acceleration is the largest. Also, in this case, the PCA $\alpha_\oplus$ varies in a wide range, from 0 to 90 deg, thus yielding considerable BBRP accelerations. While these considerations hold true also for the spherical models, their error bands exhibit a weaker dependency with the LTAN. This stems from the fact that the spherical models manage to approximate the ARP and BBRP accelerations better than the no-PRP and FD models, particularly for LTANs close to 0000/1200 hrs. Although the errors that the uniform and sinusoidal models produce are similar in magnitude, it is worth noting that the width of the uniform model's error band is larger than the sinusoidal model's error band. This is due to the higher level of approximation of the uniform model, which introduces a larger error uncertainty with respect to the simulation start time. The narrower error band displayed by the sinusoidal model also highlights its different trend compared to the other models, with a minimum for a LTAN at 0000/1200 hrs and a maximum for LTANs close to 0600/1800 hrs. This trend is determined by a second-order source of error, originating from a complex interplay between the sail orientation and the Sun-Earth-sailcraft relative geometry. Indeed, when the day-night terminator is visible from the sailcraft and for specific sail attitudes, the outward-facing side of the sail can receive more albedo radiation than its inward-facing side. This yields an ARP acceleration that points opposite to $\hat{\boldsymbol{n}}_{\text{out}}$. However, because of the simplifying assumption that the Earth irradiates isotropically, the sinusoidal model always provides ARP accelerations pointing toward $\hat{\boldsymbol{n}}_{\text{out}}$; see Eq. (18). This discrepancy affects the results particularly if the day-night terminator is often visible from the sailcraft, that is, for a LTAN at 0600/1800 hrs, thus yielding a larger relative error ε_{rel}. Conversely, for LTANs close to 0000/1200 hrs, the day-night terminator is visible only for short periods of time, and therefore ε_{rel} is minimum.

As can be seen in the plots, neglecting the PRP acceleration in the dynamics yields large relative errors, even in the order of 14%. When employing the FD model, these errors are strongly reduced, reaching values of 4% at most. Because of their higher fidelity with respect to the FD model, the spherical models achieve even smaller errors, in the range 0–1.3% and 0.3–1% for the uniform and sinusoidal models, respectively.

Similarly as in Fig. 11 for the orbit-raising case, Fig. 12 displays the variation of ε_{rel} for the inclination-changing steering law, for different LTANs and PRP acceleration models. In this case, a 12-hour periodicity in the errors is again obtained, although the error bands appear skewed and asymmetric, unlike the ones observed in Fig. 11. This asymmetry is due to the complex, discontinuous nature of the inclination-changing steering law, for which orbits with similar orientations with respect to the sunlight direction still yield different increases in inclination [1]. Similar to the orbit-raising case, only a minor ARP acceleration perturbs the orbit for LTANs close to 0600/1800 hrs, as the phase angle is close to 90 deg at all times. This leads to small relative errors ε_{rel} particularly when the no-PRP, FD, or uniform models are used. The errors achieved by these three models increase as the LTAN deviates from 0600/1800 hrs, reaching their maximum between 1100/2300 hrs and 1400/0200 hrs. In these cases, the sail flies in the vicinity of the subsolar point once per orbit with a small PCA. This results in considerable ARP and BBRP accelerations, which yield larger errors for all models except the sinusoidal model. Indeed, for the same range of LTANs, the sinusoidal model achieves much smaller errors, even compared to the uniform model. This is due to the higher fidelity with which the blackbody and albedo radiation fluxes are modeled. As such, the error difference between the uniform and sinusoidal models provides direct insights into how the modeling of the blackbody and albedo radiation fluxes affects the accuracy. Comparing the error bands of the spherical sinusoidal and uniform models, it can be noted that the former exhibits a narrower spread than the latter. As for the orbit-raising case, this is due to the better level of approximation of the sinusoidal model, which yields a lower error uncertainty. The plots also show that the sinusoidal model achieves its maximum error for a LTAN at 0800/2000 hrs. Like in the orbit-raising case, this is due to the approximation that the Earth behaves as an isotropic radiator, which can lead to errors in the ARP acceleration direction when in proximity of the day-night terminator.

Figure 12 shows that if the PRP is not accounted for in the dynamics large errors are produced, reaching magnitudes even in the order of 34%. On the other hand, smaller errors are achieved when the FD, spherical uniform, and spherical sinusoidal models are employed, reaching values of at most 5.0, 2.8, and 1.1%, respectively.

2. *Variation in Accuracy Due to Altitude*

The parametric analysis discussed in Sec. V.B.1 provided insights into the accuracy of the PRP acceleration models for a wide variety of LTANs and simulation start times. Nevertheless, the fidelity of the FD and spherical PRP acceleration models also depends on the orbital altitude considered, as highlighted in Sec. V.A. In light of this, additional parametric analyses have been conducted in order to quantify the variation in the accuracy of the PRP acceleration models with altitude. More specifically, the same parametric analyses of Sec. V.B.1 have been performed again multiple times, although considering the set of initial altitudes $h_0 = \{450, 550, 650, 715,$

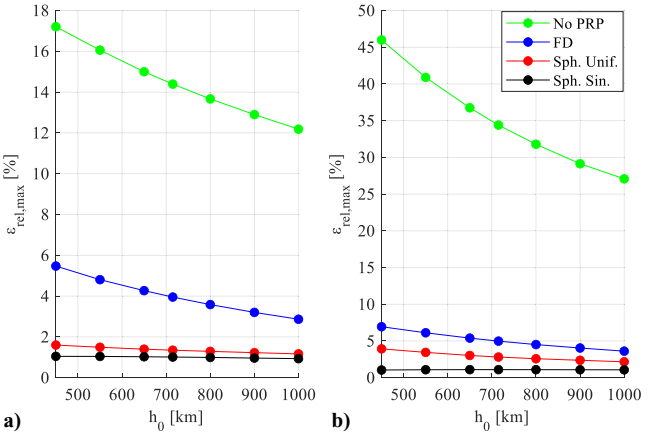

Fig. 13 Maximum relative error on the a) altitude increase and b) inclination increase for different altitudes.

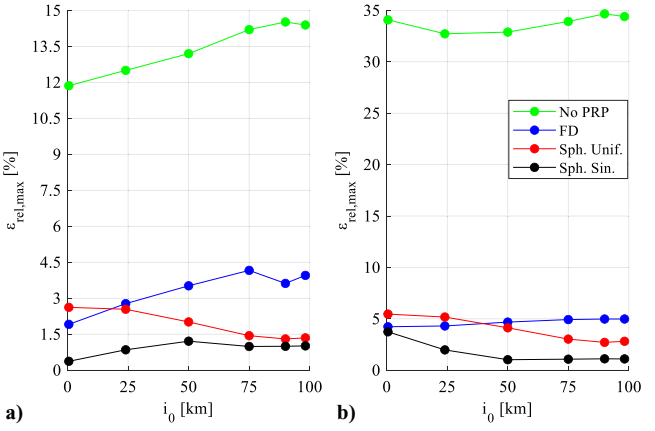

Fig. 14 Maximum relative error on the a) altitude increase and b) inclination increase for different inclinations.

800, 900, 1000} km and their corresponding Sun-synchronous inclinations, which range between $i_0 = 97.2139$ deg and $i_0 = 99.4790$ deg. It should be noted that the altitude lower bound of 450 km was chosen, as this represents the lowest altitude for which solar sails can maneuver without deorbiting, despite the intense atmospheric drag [19]. To conveniently summarize the results obtained, Fig. 13 displays the maximum relative error achieved over all LTANs and simulation start times, $\varepsilon_{rel,max}$, for each PRP acceleration model, steering law, and initial altitude.

Figure 13a shows the variation of $\varepsilon_{rel,max}$ with the initial altitude for the orbit-raising steering law. As can be observed, $\varepsilon_{rel,max}$ increases for decreasing values of h_0, for all PRP acceleration models. This stems from the fact that, by lowering the altitude, the sail experiences larger PRP accelerations perturbing the orbit to a larger extent. The increase in $\varepsilon_{rel,max}$ for increasingly lower h_0 is especially visible when PRP is not considered, as $\varepsilon_{rel,max}$ varies between 12.2 and 17.2%. Using the FD model yields better results, although maximum relative errors between 2.9 and 5.5% can still be achieved. The spherical PRP acceleration models also show a slight increase in error for decreasing altitudes, although much less pronounced than the FD and no-PRP models: $\varepsilon_{rel,max}$ always assumes values in the ranges 1.2–1.6% and 0.9–1.1% for the uniform and sinusoidal models, respectively. Figure 13b shows the change of $\varepsilon_{rel,max}$ with the initial altitude for the inclination-changing steering law. Similar to the orbit-raising case, the results show that the no-PRP, FD, and spherical uniform models perform less accurately for decreasing initial altitudes. Neglecting the PRP acceleration yields large maximum relative errors, particularly at low altitudes, where $\varepsilon_{rel,max}$ can even reach 45%. In contrast, the FD and uniform models perform considerably better than the no-PRP model, achieving $\varepsilon_{rel,max}$ in the ranges 3.6–6.9% and 2.2–3.9%, respectively. Ultimately, when the spherical sinusoidal model is employed, the error variation with altitude almost disappears, as $\varepsilon_{rel,max}$ remains between 1.05 and 1.10%.

3. *Variation in Accuracy Due to Inclination*

The parametric analyses discussed in Sec. V.B.2 provided insights into the accuracy of the PRP acceleration models for a variety of orbital conditions, though only considering Sun-synchronous orbits. Therefore, to investigate also the impact of inclination on the accuracy of the different PRP acceleration models, additional parametric analyses have been conducted. In particular, the same parametric analyses of Sec. V.B.1 have been performed again multiple times considering the inclinations $i_0 = \{0.5, 24, 50, 75, 90, 98.2490\}$ deg, where the last value corresponds to the Sun-synchronous inclination for $h_0 = 715$ km.

Figure 14a shows the variation of $\varepsilon_{rel,max}$ with the initial inclination for the orbit-raising steering law. As can be seen, neglecting the PRP acceleration leads to considerable errors, with values of $\varepsilon_{rel,max}$ even in the order of 14% for (quasi-)polar orbits. For equatorial orbits, the FD model performs particularly well, and, notably, it achieves $\varepsilon_{rel,max}$ even lower than the uniform model's. However, for increasing initial inclinations, the accuracy of the FD model reduces, while that of the uniform model improves. This causes the error curve of the FD model to grow from 1.9 to a maximum of 4.2%, whereas for the uniform model, $\varepsilon_{rel,max}$ reduces from 2.6 to 1.3%. The uniform model displays large errors for small inclinations because of its limited accuracy in predicting the planetary radiation flux near the equator. Because the sailcraft flies only on top of the equatorial region for an equatorial orbit, the error committed accumulates rapidly over time. On the other hand, for larger inclinations, the sailcraft's ground track covers a larger portion of the Earth's surface, thus alleviating the accumulation of error and lowering $\varepsilon_{rel,max}$. Ultimately, the sinusoidal model achieves the lowest errors for any initial inclination considered, with $\varepsilon_{rel,max}$ varying in the range 0.4–1.2%. Figure 14b shows the change of $\varepsilon_{rel,max}$ with the initial inclination for the inclination-changing steering law. The error curves of the no-PRP model shows a weak dependency with the initial inclination, whereas the FD and uniform models display trends similar to those found in Fig. 14a. Compared to the orbit-raising case, however, the magnitude of the errors is amplified: $\varepsilon_{rel,max}$ reaches even 34.7% when PRP is neglected, while values in the ranges 4.2–5.0% and 2.7–5.5% are found for the FD and uniform models, respectively. Unlike Fig. 14a, the sinusoidal model performs worse for equatorial orbits than high-inclination orbits, as $\varepsilon_{rel,max} = 3.7\%$ is found for $i_0 = 0.5$ deg, while smaller errors of at most of 1.1% are found for (quasi-)polar inclinations. Nonetheless, the sinusoidal model still performs the best among all models and for all inclinations considered.

The results presented in Figs. 13 and 14 highlight the limits of both the FD and no-PRP acceleration models to accurately represent the solar-sail dynamics, especially at low altitudes and for orbits with high inclination. On the other hand, the spherical uniform and sinusoidal models achieve much lower errors, with the sinusoidal model performing the best among all analytical models, as it achieves a consistent accuracy independent of altitude and only slightly dependent on inclination. Based on these results, therefore, the spherical uniform and sinusoidal models are deemed validated. In addition to their accuracy, it should also be noted that using the spherical uniform or sinusoidal models incurs only minor additional computational costs compared to the FD model. This is due to the fact that all these models are analytical. Therefore, they require a similar computational effort which is, however, substantially smaller than the computational effort required by numerical methods such as NRTDM. More specifically, by considering several orbital scenarios and computing the corresponding PRP accelerations through the aforementioned models, it was found that the spherical sinusoidal model requires run times 1.02 and 2.73 times larger than those of the spherical uniform and FD models, respectively. In contrast, the run time of the sinusoidal model was found to be 31.7 times shorter than the run time of the NRTDM model.

VI. ACS3 Mission Analysis

In this section, the effect of the BBRP and ARP accelerations on the orbit-raising and inclination-changing capabilities of different Earth-bound solar-sail orbits is analyzed. Similar to the last section, all analyses make use of the ACS3 mission as baseline scenario, with a simulation start time of 1 June 2024 (i.e., the expected deployment date of the solar sail). The initial orbital elements are given in Eq. (41), although the initial LTAN values have been restricted to 0600 and 1200 hrs only. These identify two orbits in dawn-dusk and noon-midnight conditions, corresponding to right ascensions of the ascending node of 339.9554 and 69.9554 deg, respectively. Unlike Sec. V (in which the dynamics considered only the SRP and PRP accelerations), in this section, a more realistic full-dynamical model is employed, which accounts also for the aerodynamic and J_2 gravitational accelerations. In these dynamics, the PRP acceleration is modeled using the spherical sinusoidal model, because of its high accuracy and limited computational costs, as seen in Sec. V. For each initial orbit, the solar-sail dynamics are propagated, and locally optimal orbit-raising and inclination-changing steering laws are employed. These steering laws are computed using an algorithm accounting for SRP, atmospheric drag, and the J_2 perturbation in the optimization process [19], but not for the PRP. Therefore, the BBRP and ARP accelerations are considered as uncontrolled perturbing accelerations affecting the orbit. To quantify the effect of these accelerations on the orbit-raising and inclination-changing capabilities of the ACS3 mission, the equations of motion presented in Eq. (1) are propagated with and without PRP acceleration on the right-hand side. In this way, the final increases in altitude and inclination for PRP-perturbed and PRP-unperturbed orbits can be compared and their differences assessed. Similarly as in Sec. V, for each scenario, the equations of motion are propagated for 10 days using MATLAB®'s ode45 integrator, with absolute and relative tolerances of 10^{-12}. More details on the optimization scheme as well as the settings used for the optimizer are provided in Ref. [19].

Figure 15 shows the variation of the SRP, aerodynamic, BBRP, and ARP accelerations over one orbital period, for the orbit-raising and inclination-changing steering laws (top and bottom plots, respectively) and LTANs at 0600 and 1200 hrs (left and right plots, respectively). It should be noted that, although the J_2 gravitational acceleration has also been included in the dynamics, its magnitude is not displayed in Fig. 15. This is because the J_2 acceleration is significantly larger than the other accelerations considered, ranging between 206 and 459 times the characteristic acceleration a_c. The large differences in the acceleration profiles for the four cases are due to the different sail attitude control profiles adopted. Indeed, the solar-sail attitude control is computed through the optimization process and strongly depends on the steering law and LTAN considered [19]. As shown in the plots, most of the time, the SRP acceleration is the dominant acceleration. However, the BBRP and ARP accelerations can get as large as 10–15% of the solar-sail characteristic acceleration and, for some cases and in some particular sections of the orbit, attain values even larger than the SRP acceleration. These large values of the BBRP and ARP accelerations are achieved when an initial LTAN of 1200 hrs is considered. As discussed in Sec. V, this is due to the orbit orientation (which allows the sailcraft to fly in proximity of the subsolar point) and the low PCA values encountered along the orbit. On the other hand, for an initial LTAN at 0600 hrs, the PCA and phase angle assume values close to 90 deg, thus yielding smaller BBRP and ARP accelerations equal to at most 4% of the characteristic acceleration. It is interesting to note that when an orbit-raising steering law is considered, no BBRP and ARP accelerations are produced during eclipses. Indeed, in this circumstance, the normal vector of the sail is oriented perpendicular to the orbital plane. This translates into the sail being oriented parallel to the wind flow to prevent atmospheric drag while, at the same time, the BBRPs on the sail front and back sides counteract each other to produce a null net acceleration. In addition, because the sail is in eclipse, no solar radiation or albedo is present, thus making the total acceleration exerted on the sail reduce to the J_2 acceleration only. When an inclination-changing steering law is employed and the sail is in eclipse, a similar phenomenon takes

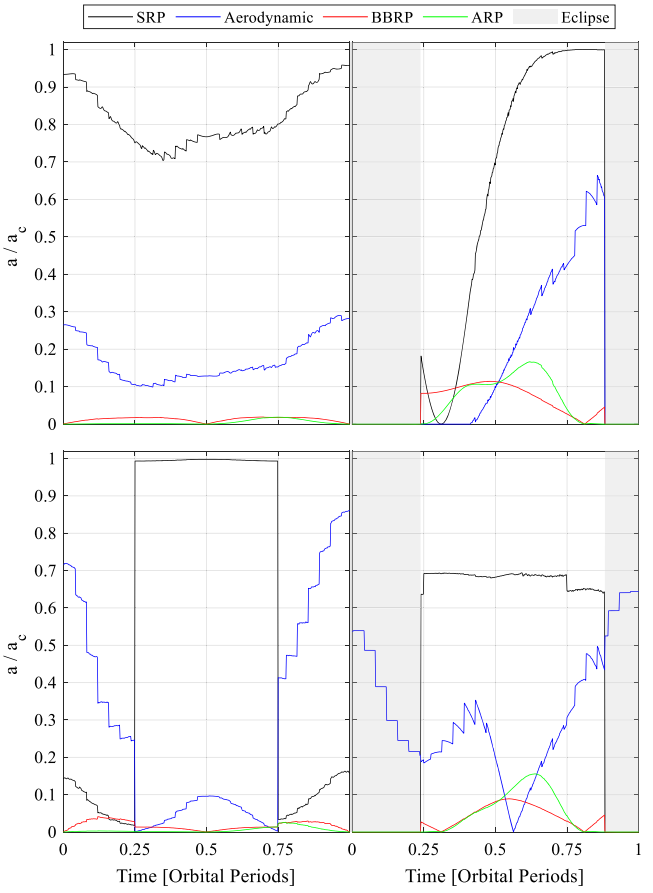

Fig. 15 ACS3 acceleration profiles for the orbit-raising (top) and inclination-changing (bottom) steering laws with LTAN at 0600 (left) and 1200 hrs (right).

place. Indeed, in this case, the sail is oriented edgewise with respect to the radial direction, but with a nonzero angle of attack with respect to the wind flow. As a consequence, this sail attitude yields once again a null BBRP acceleration but also a nontrivial aerodynamic acceleration. This is visible in the bottom-right plot of Fig. 15 for the inclination-changing steering law with LTAN at 1200 hrs, which shows that the aerodynamic acceleration is the only nonzero acceleration (except for the J_2 acceleration, not displayed).

Table 1 displays the average BBRP and ARP accelerations experienced by the sail and the final altitude and inclination increases obtained after 10 days, for all orbit scenarios, with and without PRP in the dynamics. In the table, $\Delta\text{œ}$ is the total increase in the steering law's target parameter (i.e., h or i) after 10 days, and $\varepsilon_{\text{rel},f}$ is the relative error between the $\Delta\text{œ}$ found with and without PRP in the dynamics. It should be noted that, although the J_2 acceleration is orders of magnitudes larger than the SRP, PRP, or aerodynamic accelerations, the results given in Table 1 are affected by the J_2 perturbation only to a limited extent. Indeed, the J_2 perturbation has no secular effect on the altitude and inclination, only a short-term periodic effect [36]. Consequently, accounting for the J_2 perturbation affects the investigation of the orbit-raising and inclination-changing capabilities of solar sails only slightly. As observed also in Fig. 15, the average BBRP and ARP accelerations are considerably smaller for a LTAN at 0600 hrs than at 1200 hrs. Therefore, for a LTAN at 0600 hrs, the effect of the PRP on the orbit-raising/inclination-changing capabilities of the sail is only minor. This translates into relative errors in the altitude/inclination change in the range 0.2–0.7% with respect to the case in which the PRP is not accounted for. Conversely, for a LTAN at 1200 hrs, larger BBRP and ARP accelerations are found, and the orbit is perturbed significantly; neglecting the PRP in the dynamics yields relative errors of 24.21 and 19.61% for the orbit-raising and inclination-changing steering laws, respectively. It is interesting to note that the relative errors $\varepsilon_{\text{rel},f}$ given in Table 1 assume values close to the relative errors ε_{rel}

Table 1 ACS3 simulation results for different steering laws and initial LTANs, with and without PRP

Steering law	Orbit raising				Inclination changing			
LTAN	0600 hrs		1200 hrs		0600 hrs		1200 hrs	
PRP	✗	✓	✗	✓	✗	✓	✗	✓
$a_{\mathrm{BBRP,avg}}/a_c$, %	N/A	1.31	N/A	4.57	N/A	2.59	N/A	2.88
$a_{\mathrm{ARP,avg}}/a_c$, %	N/A	0.48	N/A	4.85	N/A	0.71	N/A	3.82
$\Delta\text{œ}$	19.581 km	19.445 km	12.834 km	10.332 km	$9.370 \cdot 10^{-2}$ deg	$9.347 \cdot 10^{-2}$ deg	$4.886 \cdot 10^{-2}$ deg	$4.085 \cdot 10^{-2}$ deg
$\varepsilon_{\mathrm{rel},f}$, %	0.701		24.21		0.246		19.61	

✓ indicates that the PRP is considered, while ✗ indicates that the PRP is not considered.

displayed in Figs. 11 and 12, for the no-PRP error band. This is due to the fact that $\varepsilon_{\mathrm{rel},f}$ is defined similarly as in Eq. (42), where the final altitude/inclination achieved by the NRTDM model, $\text{œ}_{\mathrm{NRTDM},f}$, is substituted with the final altitude/inclination of the spherical sinusoidal model. Because the difference between the final altitude/inclination achieved by these two models is minor (see again Figs. 11 and 12), $\varepsilon_{\mathrm{rel}}$ and $\varepsilon_{\mathrm{rel},f}$ assume similar values. More specifically, the values assumed by $\varepsilon_{\mathrm{rel},f}$ for the inclination-changing steering law are within or slightly below the error band of Fig. 12. On the other hand, the errors $\varepsilon_{\mathrm{rel},f}$ for the orbit-raising steering law are within the error band of Fig. 11 for a LTAN at 0600 hrs but are far above the error band for a LTAN at 1200 hrs. Further investigations showed that this discrepancy is due to the presence of the aerodynamic drag, which strongly affects the achieved altitude increase. Consequently, accounting for it in this section but not in Sec. V produces larger relative errors compared to the those of Fig. 11.

The results provided in this section show that the PRP acceleration can achieve a nonnegligible magnitude compared to the SRP and aerodynamic accelerations. When the PRP is uncontrolled, the orbit-raising and inclination-changing capabilities of solar sails can be affected negatively to a significant extent. Therefore, in future research, accounting for the PRP in the optimization procedure may prove beneficial. In this way, the detrimental effects observed in the presented analysis may be counteracted, and, potentially, even larger altitude and inclination changes might be achieved than foreseen to date.

VII. Conclusions

In this paper, a novel analytical model for the PRP accelerations of double-sided perfectly reflecting solar sails has been presented. The accuracy of this model, named the spherical PRP acceleration model, has been measured by analyzing the orbit-raising and inclination-changing capabilities of NASA's upcoming ACS3 mission under the influence of PRP, for a wide variety of orbital scenarios. The results show the spherical model's superiority in terms of accuracy compared to another state-of-the-art analytical model, namely, the finite-disk radiation pressure acceleration model devised by McInnes. Furthermore, when the spherical model is used assuming sinusoidal distributions of the Earth's blackbody radiation flux and albedo coefficient with latitude, it achieves a very high accuracy even compared to a high-fidelity numerical model, with errors at most in the order of 1 and 3% in the measured altitude and inclination gains, respectively. This accuracy is found consistently for all orbit scenarios analyzed, regardless of the orbit orientation, altitude, steering law, or time of the year considered. In addition, the spherical model was also found to require 32 times less run time than the previously mentioned numerical model. These results demonstrate the validity of the spherical model as a computationally efficient, yet accurate, alternative to numerical PRP acceleration models, particularly for planetocentric solar-sail mission design and analysis. Finally, the newly devised spherical model has also been used to determine the perturbing effect of the PRP acceleration on Earth-orbiting solar sails. Using the ACS3 mission as reference scenario, it was shown that neglecting the PRP acceleration in the dynamics can lead to large errors in the estimated orbit-raising and inclination-changing capabilities, even in the order of 20%. This result highlights the importance of accounting for the PRP acceleration in the solar-sail dynamics. Furthermore, because the PRP acceleration can reach magnitudes up to 10–20% of the solar-sail characteristic acceleration in proximity of the Earth, the results also suggest that the PRP acceleration may be exploited beneficially to enhance the maneuvering capabilities of solar sails.

Acknowledgments

The authors thank W. Keats Wilkie from NASA Langley Research Center and Andrew Heaton from NASA Marshall Space Flight Center for fruitful discussions on the ACS3 mission and valuable information shared. Also, special thanks go to Christian Siemes and Natalia Hladczuk from Delft University of Technology and Eelco Doornbos from the Koninklijk Nederlands Meteorologisch Instituut (KNMI) for sharing the software tool NRTDM and their knowledge of the ANGARA Earth radiation maps.

References

[1] McInnes, C. R., *Solar Sailing—Technology, Dynamics and Mission Applications*, Springer–Verlag, Berlin, 2004, pp. 1–11, 32–46, 112–151, Chaps. 1, 2, 4.

[2] Spencer, D. A., Johnson, L., and Long, A. C., "Solar Sailing Technology Challenges," *Aerospace Science and Technology*, Vol. 93, Oct. 2019, Paper 105276. https://doi.org/10.1016/j.ast.2019.07.009

[3] Macdonald, M., and McInnes, C. R., "Solar Sail Science Mission Applications and Advancement," *Advances in Space Research*, Vol. 48, No. 11, 2011, pp. 1702–1716. https://doi.org/10.1016/j.asr.2011.03.018

[4] Dachwald, B., "Optimal Solar-Sail Trajectories for Missions to the Outer Solar System," *Journal of Guidance, Control, and Dynamics*, Vol. 28, No. 6, 2005, pp. 1187–1193. https://doi.org/10.2514/1.13301

[5] Niccolai, L., Quarta, A. A., and Mengali, G., "Solar Sail Heliocentric Transfers with a Q-Law," *Acta Astronautica*, Vol. 188, Nov. 2021, pp. 352–361. https://doi.org/10.1016/j.actaastro.2021.07.037

[6] Mengali, G., and Quarta, A. A., "Optimal Three-Dimensional Interplanetary Rendezvous Using Non-Ideal Solar Sail," *Journal of Guidance, Control, and Dynamics*, Vol. 28, No. 1, 2005, pp. 173–177. https://doi.org/10.2514/1.8325

[7] Heiligers, J., and McInnes, C. R., "Solar Sail Heliocentric Earth-Following Orbits," *Journal of Guidance, Control, and Dynamics*, Vol. 38, No. 5, 2015, pp. 937–944. https://doi.org/10.2514/1.G000579

[8] Whorton, M., Heaton, A., Pinson, R., Laue, G., and Adams, C., "NanoSail-D: The First Flight Demonstration of Solar Sails for Nanosatellites," *22nd Annual AIAA/USU Conference on Small Satellites*, Utah State Univ. Press, Logan, UT, 2008, Paper SSC08-X-1.

[9] Betts, B., Nye, B., Greeson, E., Vaughn, J., Chute, R., Spencer, D., Ridenoure, R., Munakata, R., Wong, S., Diaz, A., et al., "LightSail 1 Mission Results and Public Outreach Strategies," *Proceedings of the 4th International Solar Sailing Symposium*, Japan Space Forum, Tokyo, Japan, 2017, Paper 17093.

[10] Spencer, D. A., Betts, B., Bellardo, J. M., Diaz, A., Plante, B., and Mansell, J. R., "The LightSail 2 Solar Sailing Technology Demonstration," *Advances in Space Research*, Vol. 67, No. 9, 2021, pp. 2878–2889. https://doi.org/10.1016/j.asr.2020.06.029

[11] Pezent, J., Soon, R., and Heaton, A., "High-Fidelity Contingency Trajectory Design and Analysis for NASA's Near-Earth Asteroid (NEA) Scout Solar Sail Mission," *Acta Astronautica*, Vol. 159, June 2019, pp. 385–396. https://doi.org/10.1016/j.actaastro.2019.03.050

[12] Macdonald, M., *Advances in Solar Sailing*, Springer–Verlag, Berlin, 2014, pp. 95–113.
[13] Wilkie, W., Fernandez, J., Stohlman, O., Schneider, N., Dean, G., Kang, J., Warren, J., Cook, S., Brown, P., Denkins, T., et al., "An Overview of the NASA Advanced Composite Solar Sail (ACS3) Technology Demonstration Project," *AIAA Scitech 2021 Forum*, AIAA Paper 2021-1260, 2021.
[14] Miguel, N., and Colombo, C., "Planar Orbit and Attitude Dynamics of an Earth-Orbiting Solar Sail Under J2 and Atmospheric Drag Effects," *Advances in the Astronautical Sciences*, Vol. 167, Jan. 2018, pp. 299–319.
[15] Miguel, N., and Colombo, C., "Deorbiting Spacecraft with Passively Stabilised Attitude Using a Simplified Quasi-Rhombic-Pyramid Sail," *Advances in Space Research*, Vol. 67, No. 9, 2021, pp. 2561–2576. https://doi.org/10.1016/j.asr.2020.03.028
[16] Colombo, C., Rossi, A., Dalla Vedova, F., Braun, V., Bastida Virgili, B., and Krag, H., "Drag and Solar Sail Deorbiting: Re-Entry Time Versus Cumulative Collision Probability," *68th International Astronautical Congress*, International Astronautical Federation, 2017, pp. 3535–3553.
[17] Ionel, A., "Deorbiting Upper-Stages in LEO at EOM Using Solar Sails," *INCAS Bulletin*, Vol. 9, No. 2, 2017, pp. 117–132. https://doi.org/10.13111/2066-8201
[18] Roberts, P. C. E., and Harkness, P. G., "Drag Sail for End-of-Life Disposal from Low Earth Orbit," *Journal of Spacecraft and Rockets*, Vol. 44, No. 6, 2007, pp. 1195–1203. https://doi.org/10.2514/1.28626
[19] Carzana, L., Visser, P., and Heiligers, J., "Locally Optimal Control Laws for Earth-Bound Solar Sailing with Atmospheric Drag," *Aerospace Science and Technology*, Vol. 127, Aug. 2022, Paper 107666. https://doi.org/10.1016/j.ast.2022.107666
[20] Mengali, G., and Quarta, A. A., "Near-Optimal Solar-Sail Orbit-Raising from Low Earth Orbit," *Journal of Spacecraft and Rockets*, Vol. 42, No. 5, 2005, pp. 954–958. https://doi.org/10.2514/1.14184
[21] Stolbunov, V., Ceriotti, M., Colombo, C., and McInnes, C. R., "Optimal Law for Inclination Change in an Atmosphere Through Solar Sailing," *Journal of Guidance, Control, and Dynamics*, Vol. 36, No. 5, 2013, pp. 1310–1323. https://doi.org/10.2514/1.59931
[22] De Iuliis, A., Ciampa, F., Felicetti, L., and Ceriotti, M., "Sailing with Solar and Planetary Radiation Pressure," *Advances in Space Research*, Vol. 67, No. 9, 2019, pp. 2795–2811. https://doi.org/10.1016/j.asr.2019.11.036
[23] Barles, A., Ceriotti, M., Ciampa, F., and Felicetti, L., "An Optimal Steering Law for Sailing with Solar and Planetary Radiation Pressure," *Aerospace Science and Technology*, Vol. 118, Nov. 2021, Paper 107051. https://doi.org/10.1016/j.ast.2021.107051
[24] Lautman, D. A., "Perturbations of a Close-Earth Satellite Due to Sunlight Diffusely Reflected from the Earth-I: Uniform Albedo," *Celestial Mechanics*, Vol. 15, No. 4, 1977, pp. 387–420. https://doi.org/10.1007/BF01228609
[25] Lautman, D. A., "Perturbations of a Close-Earth Satellite Due to Sunlight Diffusely Reflected from the Earth-II: Variable Albedo," *Celestial Mechanics*, Vol. 16, No. 1, Sept. 1977, pp. 3–25. https://doi.org/10.1007/BF01235724
[26] Borderies, N., and Longaretti, P.-Y., "A New Treatment of the Albedo Radiation Pressure in the Case of a Uniform Albedo and of a Spherical Satellite," *Celestial Mechanics and Dynamical Astronomy*, Vol. 49, No. 1, 1990, pp. 69–98. https://doi.org/10.1007/BF00048582
[27] Borderies, N., "A General Model of the Planetary Radiation Pressure on a Satellite with a Complex Shape," *Celestial Mechanics and Dynamical Astronomy*, Vol. 49, No. 1, March 1990, pp. 99–110. https://doi.org/10.1007/BF00048583
[28] Senhal, L., "Effects of the Terrestrial Infrared Radiation Pressure on the Motion of an Artificial Satellite," *Celestial Mechanics*, Vol. 25, No. 2, 1981, pp. 169–179. https://doi.org/10.1007/BF01230517
[29] Rubincam, D. P., and Weiss, N. R., "Earth Albedo and the Orbit of LAGEOS," *Celestial Mechanics*, Vol. 38, No. 3, 1986, pp. 233–296. https://doi.org/10.1007/BF01231110
[30] Abd El-Salam, F. A., and Sehnal, L., "The Effects of the Terrestrial Infrared Radiation Pressure on the Earth's Artificial Satellite Dynamics," *Applied Mathematics and Computation*, Vol. 162, No. 3, 2005, pp. 1431–1451. https://doi.org/10.1016/j.amc.2004.03.019
[31] Baker, R. M. L., Jr., "Radiation on a Satellite in the Presence of Partly Diffuse and Partly Specular Reflecting Body," *Trajectories of Artificial Celestial Bodies/Trajectoires des Corps Celestes Artificiels*, edited by J. Kovalevsky, Springer–Verlag, Berlin, 1966, pp. 85–150. https://doi.org/10.1007/978-3-642-49326-3_14
[32] Gini, F., Bardella, M., and Casotto, S., "Precise Non-Gravitational Forces Modeling for GOCE," *Advances in the Astronautical Sciences*, Vol. 152, Jan. 2014, pp. 3141–3157.
[33] Putney, B., Kolenkiewicz, R., Smith, D., Dunn, P., and Torrence, M., "Precision Orbit Determination at the NASA Goddard Space Flight Center," *Advances in Space Research*, Vol. 10, Nos. 3–4, 1990, pp. 197–203. https://doi.org/10.1016/0273-1177(90)90350-9
[34] Arnold, S. J., and Dow, J. M., "Models for Spacecraft Acceleration Due to Earth Albedo and Infrared Radiation," European Space Operations Centre (ESOC) OAD WP 265, 1984.
[35] Doornbos, E., Bruinsma, S., Fritsche, B., Koppenwallner, G., Visser, P., Van Den Ijssel, J., and de Encarnação, J. D. T., "Algorithm Theoretical Basis Document," GOCE+ Theme 3: Air Density and Wind Retrieval Using GOCE Data, ESA CR 4000102847/NL/EL, 2014.
[36] Wertz, J. R., and Larson, W. J., *Space Mission Analysis and Design*, Kluwer Academic, Norwell, MA, 2005, pp. 142–144, 897–898, Chap. 6.
[37] Wakker, K. F., *Fundamentals of Astrodynamics*, Delft Univ. of Technology, Institutional Repository, Delft, The Netherlands, 2015, pp. 527–554, Chap. 20.
[38] Ortiz Longo, C. R., and Rickman, S. L., "Method for the Calculation of Spacecraft Umbra and Penumbra Shadow Terminator Points," NASA Center for AeroSpace Information, 1995.
[39] Kelly, P., and Bevilacqua, R., "An Optimized Analytical Solution for Geostationary Debris Removal Using Solar Sails," *Acta Astronautica*, Vol. 162, Sept. 2019, pp. 72–86. https://doi.org/10.1016/j.actaastro.2019.05.055
[40] Tiesinga, E., Mohr, P. J., Newell, D. B., and Taylor, B. N., "CODATA Recommended Values of the Fundamental Physical Constants: 2018," *Reviews of Modern Physics*, Vol. 93, No. 2, June 2021, Paper 033105. https://doi.org/10.1103/RevModPhys.93.025010
[41] Storch, J. A., *Aerodynamic Disturbances on Spacecraft in Free-Molecular Flow*, Aerospace Corp., El Segundo, CA, 2002, p. 9, Chap. 2.
[42] Atchison, J. A., and Peck, M. A., "Length Scaling in Spacecraft Dynamics," *Journal of Guidance, Control, and Dynamics*, Vol. 34, No. 1, 2011, pp. 231–246. https://doi.org/10.2514/1.49383
[43] Nerem, R. S., Lerch, F. J., Marshall, J. A., Pavlis, E. C., Putney, B. H., Tapley, B. D., Eanes, R. J., Ries, J. C., Schutz, B. E., Shum, C. K., et al., "Gravity Model Development for TOPEX/POSEIDON: Joint Gravity Models 1 and 2," *Journal of Geophysical Research*, Vol. 99, No. C12, 1994, pp. 24,421–24,447. https://doi.org/10.1029/94JC01376
[44] Carroll, B. W., and Ostlie, D. A., *An Introduction to Modern Astrophysics*, Cambridge Univ. Press, Cambridge, England, U.K, 2017, pp. 263–269, Chap. 9. https://doi.org/10.1017/9781108380980
[45] Lissauer, J., and de Pater, I., *Fundamental Planetary Science: Physics, Chemistry and Habitability*, Cambridge Univ. Press, Cambridge, England, U.K., 2013, pp. 87–90, Chap. 4.
[46] Cunningham, F. G., *Power Input to a Small Flat Plate from a Diffusely Radiating Sphere, with Application to Earth Satellites*, NASA, 1961, pp. 2–3.
[47] Fritsche, B., Ivanov, M., Kashkovsky, A., Koppenwallner, G., Kudryavtsev, A., Voskoboinikov, U., and Zhukova, G., "Radiation Pressure Forces on Complex Spacecraft," European Space Operations Centre (ESOC) CR 11908, 1998.
[48] Doornbos, E., *Thermospheric Density and Wind Determination from Satellite Dynamics*, Springer–Verlag, Berlin, 2012.
[49] Doornbos, E., Scharroo, R., Zandbergen, R., and Klinkrad, H., "Improved Modelling of Surface Forces in the Orbit Determination of ERS and ENVISAT," *Canadian Journal of Remote Sensing*, Vol. 28, No. 4, 2002, pp. 535–543. https://doi.org/10.5589/m02-055
[50] Thornton, E. A., *Thermal Structures for Aerospace Applications*, AIAA, Reston, VA, 1996, pp. 29–34, Chap. 2.